A WIND TUNNEL STUDY OF TURBULENT FLOW AROUND SINGLE AND MULTIPLE WINDBREAKS, PART I: VELOCITY FIELDS

M. J. JUDD[1], M. R. RAUPACH[2] and J. J. FINNIGAN[2]
[1]*Horticultural and Food Research Institute of NZ, PO Box 23, Kerikeri, New Zealand;*
[2]*CSIRO Centre for Environmental Mechanics, GPO Box 821, Canberra, ACT 2601, Australia*

(Received in final form 26 March, 1996)

Abstract. This paper describes wind-tunnel experiments on the flow around single and multiple porous windbreaks (height H), sheltering a model plant canopy (height $H/3$). The mean wind is normal to the windbreaks, which span the width of the wind tunnel. The incident turbulent flow simulates the adiabatic atmospheric surface layer. Five configurations are examined: single breaks of three solidities (low, medium, high; solidity = 1 − porosity), and medium-solidity multiple breaks of streamwise spacing $12H$ and $6H$. The experimental emphases are on the interactions of the windbreak flow with the underlying plant canopy; the effects of solidity; the differences in shelter between single and multiple windbreaks; and the scaling properties of the flow. Principal results are: (1) the "quiet zones" behind each windbreak are smaller in multiple than single arrays, because of the higher turbulence level in the very rough-wall internal boundary layer which develops over the multiple arrays. Nevertheless, the overall shelter effectiveness is higher for multiple arrays than single windbreaks because of the "nonlocal shelter" induced by the array as a whole. (2) The flow approaching the windbreak decelerates above the canopy but accelerates within the canopy, particularly when the windbreak solidity is high. (3) A strong mixing layer forms just downwind of the top of each windbreak, showing some of the turbulence and scaling properties of the classical mixing layer formed between uniform, coflowing streams. (4) No dramatic increase in turbulence levels in the canopy is evident at the point where the deepening mixing layer contacts the canopy (around $x/H = 3$) but the characteristic inflection in the canopy wind profile is eliminated at this point.

1. Introduction

Windbreaks have been used by agriculturalists for hundreds, if not thousands, of years. However, they remain the subject of active research for the simple reason that we are not yet able to predict their aerodynamic performance reliably, let alone their effect on plant production. This is partly due to a wide range of practical motivations for windbreak research, spanning agriculture, forestry, soil conservation and other applied fields. Hence, although there has been a plethora of experiments in specific contexts, systematic generalisation has been difficult (Baltaxe, 1967).

From an aerodynamic perspective, recent overviews of experimental windbreak research include those by Plate (1971a,b), Raine and Stevenson (1977), McNaughton (1988) and Heisler and De Walle (1988). Fluid mechanical studies of the separated flow behind a bluff plate at the leading edge of a splitter plate (Ruderich and Fernholz, 1986; Castro and Haque, 1987, 1988) are also of some relevance. Theoretical and modelling work includes that of Counihan *et al.* (1974), a perturbation solution for the velocity field in the far wake of a solid barrier: Wilson (1985), a numerical investigation of windbreak flow using several turbulence

Boundary-Layer Meteorology **80:** 127–165, 1996.

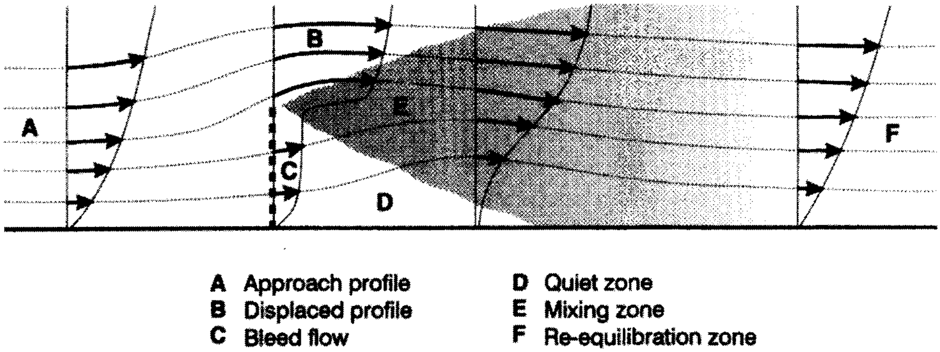

Figure 1. Schematic diagram of two-dimensional flow field around a windbreak, showing the six flow zones used in this paper. Horizontal and vertical axes are not to same scale.

closure schemes; and Wilson *et al.* (1990), a perturbation analysis of the turbulent flow through a porous barrier.

The above work has established many of the general observed features of flows around windbreaks. However, it also indicates several areas where continuing research is required, including three-dimensional windbreak flows, scalar transfers in the windbreak environment, the effects of upstream conditions such as roughness, the effects of multiple windbreaks, and the aerodynamic interaction between a windbreak and the (shorter) crop which it shelters. The present experimental investigation is aimed particularly at the last two of these areas.

We consider the "two-dimensional" case in which the mean wind is normal to a long, uniform windbreak. Some well-known features of this flow are:

(1) The flow may be divided into several fluid-mechanically distinct zones (done in slightly different ways by different authors: e.g. Plate, 1971a; Raine and Stevenson, 1977). We use the six zones shown in Figure 1: the upwind *approach profile*; the *displaced flow* above the barrier; the *bleed flow* through a porous barrier; a sheltered *quiet zone* extending upwind to $x/H \approx -1$ and downwind to $x/H \approx 3 - 7$ (where H is the windbreak height and x is downwind distance); a strongly turbulent *mixing zone* (sometimes called a wake zone) above and downwind of the quiet zone; and, further downwind, a *re-equilibration zone* in which the flow perturbations induced by the windbreak are smoothed out until the approach flow is re-established.

(2) Outside of a region just downwind of the break, the physical structure of windbreaks appears to have minimal effect beyond that associated with their porosity (Perera, 1981), although low-level gaps can create a local low-level jet close to the windbreak (Sturrock, 1969). Windbreak porosity β is an optical measure defined as the ratio of open to total area, as seen from the wind direction; an equivalent measure is the solidity $\sigma = 1 - \beta$, the ratio of solid to total area (this is sometimes called the windbreak density).

(3) Accumulated evidence (Van Eimern *et al.,* 1964; Perera, 1981; Guyot, 1986) points to recirculation in the quiet zone for windbreaks of porosity $\lesssim 0.3$ or solidity $\gtrsim 0.7$. Decreasing solidity, while not much affecting the shape of the quiet zone or recirculation region, increases the minimum wind speed in the lee and moves the point of minimum wind speed downstream (Castro, 1971; Hagen and Skidmore, 1971; Bean *et al.,* 1975).

(4) Windbreak height and solidity (particularly the solidity at the base of the windbreak) have long been recognised as prime determinants of sheltered area (Sturrock, 1969; Gandemer, 1981). More recently, turbulence in the approach flow has also been identified as exerting an influence, particularly in the near lee (Hagen and Skidmore, 1971; Raine and Stevenson, 1977; Gandemer, 1981; Wilson, 1987). The importance of the upwind roughness (z_0), and the dimensionless scaling parameter H/z_0, have long been recognised for modelling purposes (Jensen, 1958; Raine and Stevenson, 1977). However, few field experimental studies have examined this dependence (McNaughton, 1988). Experimental parameters range from $H/z_0 < 40$ to $H/z_0 > 10^4$, with the majority of field experiments in the range $100 < H/z_0 < 1000$, corresponding with field crops or pasture in association with a windbreak some metres tall. Qualitatively, greater upstream roughness may be expected to increase the ambient turbulence and hence the rate of turbulent transfer in the lee of a windbreak, reducing the extent, and perhaps degree, of shelter. Plate (1971b) and Wang *et al.* (1990) have both described the leeward flow using Schlichting's (1968) analysis of a mixing layer. Prior to that, Konstantinov and Struzer (1965) discussed the transport processes around a windbreak by assuming that the effective eddy diffusivity was proportional to the local standard deviation of vertical wind speed and eddy size.

In agricultural or horticultural practice, windbreaks often occur in multiple arrays. There are limited data on the performance of such ensembles (Woodruff and Zingg, 1955; Van Eimern *et al.,* 1964: Gandemer, 1981; McAneney and Judd, 1991). It may be expected that the large-scale effect of multiple windbreaks would be to increase the roughness of the entire region, thereby (1) increasing the turbulence intensity and so reducing the effectiveness of individual windbreaks, and (2) decreasing the regionally averaged wind speed, inducing "nonlocal shelter". Such effects were observed by Iqbal *et al.* (1977), Seguin and Gignoux (1974) and Guyot and Seguin (1975); they found that, when one windbreak within a multiple array is compared with an equivalent isolated windbreak, there is a reduction in the extent of the most protected zones and an increase in the more poorly protected area, consistent with the suggested mechanisms. It is also common practice for single or multiple windbreaks to occur in conjunction with a rough crop. The resulting aerodynamic interaction between windbreak and crop has not been studied extensively (but see Nord, 1991 for one of the few studies available).

This paper describes wind tunnel experiments on the turbulent flow around single and multiple windbreaks, in association with a model plant canopy. The aim is to focus on some of the gaps in present understanding of windbreak flows, including the dynamics of the flow around both single and multiple windbreaks, the scaling laws which operate in the various flow zones, and the interactions with flow in the underlying plant canopy. Our interest in scaling lies in characterising some key parts of a windbreak flow (Figure 1) in terms of well-known classes of flows such as boundary layers and mixing layers, with the goal of generalising our results using scaling laws appropriate to these flow classes.

In the experiments, the incident turbulence is a simulation of the neutrally-stratified atmospheric surface layer, and the crop and windbreak heights correspond with a naturally sheltered orchard (McAneney and Judd, 1987). The work encompasses single windbreaks of three solidities, together with two multiple windbreak configurations. This paper describes the mean and turbulent velocity fields, with particular attention to scaling issues. A subsequent paper will examine turbulence and momentum budgets, spectra, length scales and drag. In the rest of the paper, "windbreak" and "break" are used synonymously.

2. Experimental Configurations and Methods

2.1. CONFIGURATIONS

The experiments were performed in the CSIRO Pye Laboratory wind tunnel (Wooding, 1968), an open return blower tunnel designed to simulate the flow in the neutral atmospheric surface layer. The working section (at the time of these experiments) was of length 10.1 m, width 1.8 m and height approximately 0.7 m. A flexible roof in the working section allows for some adjustment of longitudinal pressure gradients; this was done by procedures described later.

The tunnel arrangement is shown in Figure 2. On entering the working section, the flow was tripped by a 50 mm fence. The boundary layer then developed over two roughness sections (each 600 mm in length) constructed of 15 mm gravel glued to wooden baseboards (Mulhearn and Finnigan, 1978). These, and all subsequent roughness elements, completely filled the width of the tunnel. The second of these sections sloped upwards so that its zero-plane matched that of the following canopies. Following the gravel, the flow passed over a deep canopy of aluminium strips (as used by Raupach *et al.*, 1986) before meeting the flexible model wheat canopy within which the windbreaks were placed. The aluminium strips have a similar roughness to the model wheat canopy and were used both upwind and downwind of it, because of the limited availability of the model wheat (3390 mm length in the tunnel). Following the model wheat was a further 1155 mm of the aluminium strips and finally 3057 mm of the elevated gravel.

The model wheat canopy has been described in detail elsewhere (Finnigan and Mulheam, 1978; Brunet *et al.*, 1994). It consists of flexible threads of nylon monofilament (length 50 mm, diameter 0.25 mm) placed at 5 mm square spacings. Its aeroelastic properties permit simulation of a range of canopies (crop, forest,

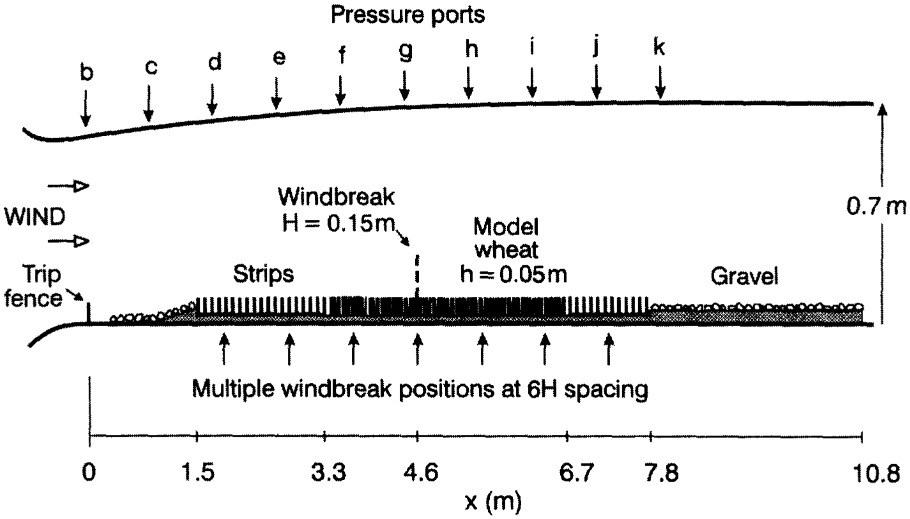

Figure 2. The wind tunnel arrangement, with the windbreak shown in the single-break test position.

other) depending on geometrical and aerodynamic scaling. Because of its natural tendency to bend, the average "aerodynamic" canopy height (h) is 47 mm. The zero plane displacement of the model wheat was matched with that of the preceding and following aluminium strips by raising its base.

Streamwise and vertical position are respectively x (positive downstream) and z (positive upwards); coordinate origins are the position of the windbreak being measured ($x = 0$) and the ground surface beneath the model wheat ($z = 0$). The lateral coordinate y forms a right-handed coordinate system (x, y, z). The instantaneous streamwise and vertical velocity components (U, W) are decomposed into local temporal means (denoted by overbars) and fluctuations therefrom (denoted by small letters): $U = \bar{U} + u$, $W = \bar{W} + w$.

The model windbreaks were of height H = 150 mm (just over 3 times the canopy height h). Solidity was always uniform with height, both within and above the canopy. All windbreaks spanned the entire tunnel width. Windbreaks were constructed from brass gauze tied to frames, each consisting of two horizontal rods (diameter 6 mm) at heights of 35 and 120 mm, welded to posts at 400 mm spacings. The posts were inserted into the model wheat and aluminium strip baseboards. Two solidities of brass gauze ("coarse" and "fine") were used to create windbreaks of three solidities (henceforth "low", "medium" and "high"). The low and medium solidity breaks consisted, respectively, of single layers of coarse and fine gauzes. The high solidity break was made from two layers of the fine gauze, one attached to each side of the supporting frame. The main physical and aerodynamic parameters of the model wheat and windbreaks are given in Table I.

Five windbreak configurations were examined: three single and two multiple. The single windbreaks were of low, medium and high solidity (or density), produc-

TABLE I

Main physical and aerodynamic parameters in the experiment

Model wheat canopy:		
Stalk length	50 mm	
Stalk diameter	0.25 mm	
Stalk spacing	5 mm	
Canopy height, h	47 mm	
Frontal area index	0.47	
Available fetch in tunnel	3.4 m	
Windbreaks:		
Height, H	0.15 m	
Pressure coefficient, k (measured):		
Sld	0.54	
Smd, M12H, M6H	2.63	
Shd	5.15	
Gauzes:	Coarse	Fine
Wire diameter	0.53 mm	0.42 mm
Wire spacing	3.12 mm	1.21 mm
Porosity, $\beta = (1 - \text{diameter/spacing})^2$	0.689	0.426
Solidity, $\sigma = 1 - \beta$	0.311	0.574
Pressure coefficient, k		
Measured	0.54	2.63
Calculated from porosity	0.58	2.33
Background flow (no windbreaks):		
Mean velocity at $z = 2H, \bar{U}(2H)$	12.0 m s^{-1}	
Mean velocity at $z = H, \bar{U}(H)$	8.6 m s^{-1}	
Friction velocity, u_*	1.0 m s^{-1}	
Displacement height, d	35 mm	
Roughness length, z_0	3.8 mm	

ing configurations henceforth labelled as Sld, Smd and Shd, respectively. Single windbreaks were inserted into the model wheat 1375 mm (9H) downwind of its leading edge, leaving 2015 mm (13.4H) of wheat downwind. The multiple windbreak configurations were constructed from medium solidity windbreaks, which were spaced at either 6H or 12H; these configurations are henceforth labelled as M6H and M12H. The multiple windbreak arrays were inserted around the streamwise position used for the single windbreaks. The windbreak at this location was the "test" windbreak in the multiple array, used for most of the measurements. For the M6H configuration, there was room for three additional windbreaks downwind of the test windbreak (two within the model wheat and one in the aluminium strips) and three upwind (one within the wheat and two in the strips). For M12H, there was room for only one extra windbreak downwind and one upwind (within the aluminium strips).

The overall boundary layer depth δ was about 0.55 m at the location of the test windbreak, so $h/\delta \approx 0.09$ and $H/\delta \approx 0.26$. The use of windbreaks occupying this fraction of the boundary layer depth was necessary to obtain adequate resolution of the canopy and windbreak flows. However, we do not expect the relatively large value of H/δ to be a major limitation; its main effect is that the wind tunnel flow does not simulate the large-scale, inactive, essentially horizontal turbulent motions in the atmospheric surface layer. The active, momentum-transferring part of the turbulence spectrum is simulated acceptably to heights well above H, as confirmed later.

2.2. VELOCITY MEASUREMENTS

The velocity measurement system was similar to that used by Raupach *et al.* (1986) and Brunet *et al.* (1994). Instantaneous streamwise and vertical velocity components (U, W) were measured by a coplanar triple hot-wire probe (henceforth a "triple probe"), constructed by positioning a single vertical wire adjacent to a Dantec 55P63 X-wire probe (Legg *et al.*, 1984). The hot wires were driven by constant-temperature bridges (TSI model 1050 series). Each wire was 1 mm long and 5 μm in diameter; the lateral distance between the outermost wires was 2.5 mm. The calibration procedure for the triple probe is described later (Section 2.4). For measurements of two velocity components, the triple probe configuration outperforms a standard X-wire probe in highly turbulent flows, as it has a wider acceptance angle in the vertical (up to $\pm 80°$ compared with $\pm 40°$) and maintains a reasonable accuracy at turbulence intensities ($i_u = u/\bar{U}$) up to about 0.5, compared with less than 0.3 for an X-wire probe.

The triple probe was mounted on a traversing mechanism which allowed motorised (though manually controlled) movement of the probe in the vertical, but which had to be manually positioned in the streamwise and lateral directions. To permit the probe to descend into the model wheat without risk of breakage from stalks, small regions of the canopy were kept stalk-free with wire cages, as in Brunet *et al.* (1994). Tests with several sizes of cage suggested that this caused little disturbance to the flow in the canopy.

Despite its advantages over an X-wire probe, the triple probe is subject to several types of error (Legg *et al.*, 1984; Raupach *et al.*, 1986). The main ones are (a) rectification error due to mean flow reversal, or short-term flow reversals at high i_u; (b) contamination of the (U, W) velocity vector by V-component velocity fluctuations; (c) dispersal of heat from one hot wire onto another; and (d) loss of high-frequency resolution by temporal smoothing over sampling intervals (0.2 ms) and spatial smoothing over the measurement volume (length scale about 2.5 mm).

Errors (a), (b) and (c) cause overestimation of the mean velocity and underestimation of turbulence moments. All these errors increase with turbulence intensity

i_u, and are therefore the largest in the (possibly) recirculating regions close to the windbreaks. Because of rectification of the U component, recirculation cannot be detected by the triple probe. We therefore checked visually for evidence of recirculation both upstream and downstream of all windbreaks in the height range $h < z < H$, by using light woollen tufts on a fine probe. No visual evidence of recirculation was found in any configuration. This suggests that mean recirculations were not present, but intermittent flow reversals remain a possibility. Therefore, the velocity data in regions of low-speed flow near the break (zones C and D in Figure 1) must be interpreted with caution.

Error (d) affects high-frequency turbulence information but not the mean velocity. It is most severe in regions where the turbulence length scale is small: within the canopy and in the intense mixing zone just downwind of the break. Our spatial and temporal sampling gives adequate resolution of the dominant turbulent eddies in the canopy, and in the mixing zone except very close to the break (x/H around 0.1).

2.3. PRESSURE MEASUREMENTS

A Datametrics pressure transducer, with an accuracy of 0.1 Pa, was used to make four kinds of pressure measurement in the tunnel. Firstly, the streamwise profile of static roof pressure in the tunnel was measured at widely spaced (950 mm) roof ports (see Figure 2); the pressures at these roof ports were used to adjust the roof height to minimise streamwise pressure gradients. The adjustment was done in different ways for the multiple and single windbreak configurations. For the multiple configurations M6H and M12H (which were studied first), the roof adjustments to minimise streamwise pressure gradients were made *after* all windbreaks were positioned. After adjustment, the streamwise pressure perturbations over the wheat were approximately 0.5% of the free-stream dynamic pressure for the M6H configuration, and 1.5% for M12H configuration (though larger perturbations occurred elsewhere in the tunnel): see Figure 3. For the single configurations Sld, Smd and Shd, the limited flexibility of the roof made it impossible to adjust the roof to give a satisfactorily low roof pressure gradient with the windbreaks in place. We therefore adopted the alternative strategy of adjusting the roof to produce a minimal pressure gradient *prior* to placing any windbreak in the tunnel. A significant (but known) pressure perturbation (δP) was then induced in the tunnel by each single windbreak, negative in sign and amounting to −5%, −13% and −19% of the free-stream dynamic pressure ($\rho U_{\mathrm{I}}^2/2$) for the Sld, Smd and Shd configurations, respectively: see Figure 3. The resulting blockage effect caused the wind tunnel models to overestimate the speedup over the single windbreaks, relative to the situation without blockage. The amount of overspeeding can be estimated from the Bernoulli equation: if δ denotes a perturbation due to the roof contour, then $\delta P/\rho = -\delta(U_{\mathrm{I}}^2)/2 = -U_{\mathrm{I}}\delta U_{\mathrm{I}}$. Hence, the fractional speedup $(\delta U_{\mathrm{I}})/U_{\mathrm{I}}$ s half the normalised negative pressure perturbation $-\delta P/(\rho U_{\mathrm{I}}^2/2)$. This implies frac-

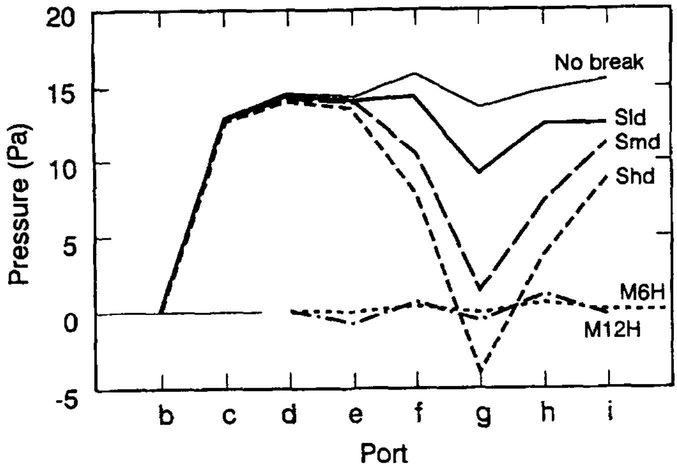

Figure 3. Static roof pressures for each configuration. M6H and M12H measured relative to port D; single break configurations relative to port B.

tional speedups of 2.5%, 6.5% and 9.5%, for the Sld, Smd and Shd configurations, respectively.

The second type of pressure measurement was a streamwise profile of the ground-level static pressure below the model wheat, on either side of the (test) windbreak and spaced upstream and downstream at intervals of $1H$. Thirdly, the pressure transducer was used in conjunction with a fine hypodermic tube to measure the pressure on both the upwind and downwind surfaces of the (test) windbreak. The tube was positioned laterally close to the gauze of the windbreak so that its open end was parallel to the flow. For Sld, the relatively large hole size makes this method uncertain because of possible contamination of the static pressure by a dynamic component. Finally, the pressure transducer was used in conjunction with a standard pitot-static tube (the same tube used for velocity calibrations) in an attempt to measure static pressure relative to an upstream roof port. These measurements were made simultaneously with the velocity profiles. The pitot-static tube was attached to the hot-wire traversing carriage at the same height as the triple probe, offset by approximately 70 mm in the lateral ($+y$) direction. Errors associated with the use of pitot-static tubes in strongly turbulent flows imply that the static pressure is overestimated by some fraction of the dynamic pressure, the fraction being small in low turbulence intensities i_u, but increasing with i_u.

Pressure coefficients (k) for each of the 3 windbreaks were measured in a small calibration tunnel with a cylindrical working section (internal diameter 60 mm). A sample of each windbreak material (coarse or fine gauze) was placed in the working section to completely cover the plane normal to the flow. The resulting pressure drop across the gauze (ΔP), together with the wind speed (U), were used to calculate k from:

$$k = \frac{2\Delta P}{\rho U^2}, \tag{1}$$

where ρ is the air density. The wind speed was calculated by measuring the pressure drop across a known constriction free from total head loss, downstream of the gauze.

The measured pressure coefficients are given in Table I. Also shown are calculated pressure coefficients for single layers of coarse and fine gauze (that is, for Sld and Smd), from the empirical formula $k = 0.52(1 - \beta^2)/\beta^2$, where β is the porosity (Laws and Livesey, 1978). The measured and empirically calculated coefficients agree to within about 15%. Henceforth the measured values are used.

2.4. DATA ACQUISITION AND PROCESSING

Vertical traverses, each consisting of between 30 and 35 levels from z = 10 mm to $z \approx$ 380 mm, were made at x-stations (streamwise positions) from upstream ($x/H = -2$) of the single windbreaks through to a maximum downstream distance of x/H = 12. For all measurements, the lateral (y) coordinate was the tunnel centreline. For the multiple windbreaks, vertical traverses were made from $x/H = -1$ through to x/H = 5 (for M6H) or 11 (for M12H), around the test windbreak location. At each level, signals from the triple probe and static pressure sensor were digitised at 5 kHz for 20 s, and recorded on magnetic tape. Time series of U and W were calculated from the triple probe signals by applying a non-linear velocity calibration to obtain instantaneous cooling velocities, and then solving for the instantaneous velocity components following the method of Legg *et al.* (1984), which takes approximate account of lateral (V component) velocity fluctuations. Additional correction factors for computed velocity moments were estimated by Legg *et al.* (1984), but these have not been applied in this experiment, following Raupach *et al.* (1986) and Brunet *et al.* (1994) who concluded that they overestimated actual errors.

A calibration for the relative angles of the hot-wires in the triple probe was made at the start of measurements on each of the five configurations. This was done in the laminar flow near the entrance to the working section, by rotating the probe through a sequence of angles in the xz plane. Highly repeatable angle calibrations were obtained. Velocity calibrations were made throughout the experiment after each 3–5 profiles, using the pitot-static tube adjacent to the triple probe; both probes were positioned at the highest point accessible with the vertical traversing mechanism ($z \approx$ 400 mm). In early experiments, the calibrations were performed without moving the probe assembly from its position in the streamwise direction (which of course changed from run to run). This procedure was used to minimise the handling of the triple probe (with attendant risk of breakage) between runs. The flow at these calibration points was not completely turbulence-free, and more importantly was also not completely horizontal ($\bar{W}/\bar{U} \neq 0$, varying from point to point) because the mean flow perturbations extended to the calibration height in the vicinity of the windbreaks. The only significant calibration error introduced by this problem was in $\bar{W}$. Once the problem was discovered, calibrations were made with the traversing mechanism as far downstream in the tunnel as possible, to remove it as far as possible from windbreak influences. For this reason, $\bar{W}$ was calculated by continuity from $\bar{U}$, as well as directly from the triple probe.

The U and W time series were used to calculate all joint moments of U and W up to third order, plus selected fourth moments. Profiles of each moment were vertically interpolated using regressive cubic splines, to produce arrays of moments and their vertical gradients on a regular grid. Streamwise gradients were calculated by fitting splines in the horizontal direction to these vertically interpolated points. Where appropriate (particularly for pressure), horizontal interpolations were made discontinuous at the windbreak. In these cases, a paucity of points upstream of the windbreak leads to poor definition of horizontal gradients there.

2.5. THE BACKGROUND FLOW

Figure 4 shows the flow characteristics over the model wheat, measured at the single-windbreak position in the absence of windbreaks. These data are very similar to those from the detailed study by Brunet *et al.* (1994) of the same canopy; see especially their "reference run". The mean velocity profile shows features typical of canopy flows (Raupach, 1988; Kaimal and Finnigan, 1994): a strong shear layer at canopy height imparts a significant inflection to $\bar{U}(z)$, at a height indistinguishable from $z = h$. Above the canopy, $\bar{U}(z)$ blends through a roughness sublayer into a nominally logarithmic profile in the inertial sublayer. The depth of the inertial sublayer is quite thin, as it is "squeezed" between the roughness sublayer (in which $\mathrm{d}\bar{U}/\mathrm{d}z$ is less than the inertial value $u_*/\kappa(z-d)$, with u_* the friction velocity, κ the von Karman constant and d the zero-plane displacement) and an outer layer in which $\mathrm{d}\bar{U}/\mathrm{d}z > u_*/\kappa(z-d)$ (Raupach *et al.*, 1986; Brunet *et al.*, 1994). This squeezing is caused by the relatively large value of h/δ, about 0.09.

Of the Reynolds stress profiles (Figure 4), the shear stress $\overline{uw}$ is approximately constant in the height range $1 < z/h \lesssim 4$. The variances $\sigma_u^2 = \overline{u^2}$ and $\sigma_w^2 = \overline{w^2}$ also vary only slowly with height in this layer. Within the canopy all stresses diminish rapidly, tending to zero at ground level. Estimating the friction velocity u_* as $(-\overline{uw})^{1/2}$ in the layer of constant shear stress, we obtain $u_* = 1.0$ m s^{-1} and hence normalised velocity standard deviations in this region of $\sigma_u/u_* = 2.3$ and $\sigma_w/u_* = 1.4$. These are very close to values from the reference run of Brunet *et al.* (1994), and compare with typical values of 2.5 and 1.25 in the neutral atmospheric surface layer (Panofsky and Dutton, 1984). Values slightly different from those in the lower atmosphere are common in laboratory simulations and may be attributed (*inter alia*) to large values of the ratio h/δ in the simulation. These small differences

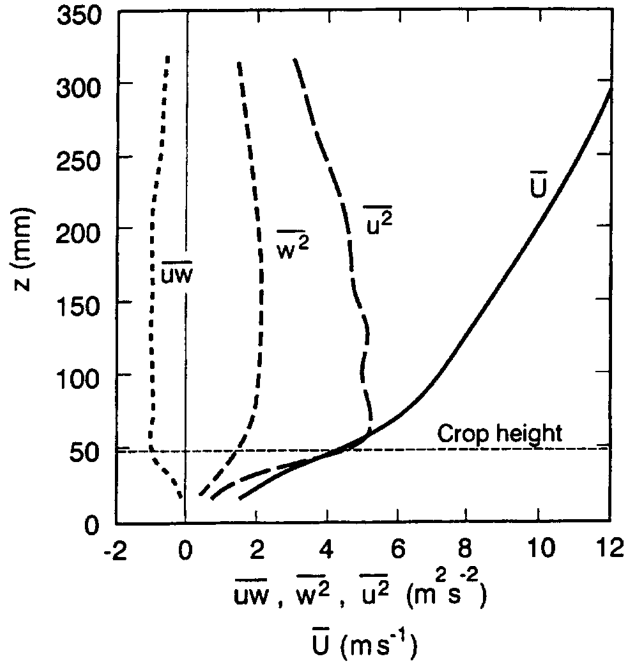

Figure 4. Background flow characteristics (without windbreaks) at the poition where the single windbreak is inserted.

aside, Figure 4 demonstrates that the background flow is an acceptable simulation of neutral atmospheric surface layer turbulence.

The zero plane displacement d was determined by the centre of pressure theorem (Thom 1971, Jackson, 1981):

$$d = \left[\int_0^h z\overline{uw}\,\mathrm{d}z\right]\left[\int_0^h \overline{uw}\,\mathrm{d}z\right]^{-1} \tag{2}$$

A small region of apparent positive $\overline{uw}$ below about $0.4h$ (almost certainly the result of measurement problems in very high-intensity turbulence) was ignored by setting $\overline{uw} = 0$ in this region when calculating the integrals in Equation (2). The result is $d = 35$ mm $= 0.74h$. The roughness length z_0 was then found by fitting the above values for u_* and d to the logarithmic mean velocity profile in the inertial sublayer:

$$\bar{U}(z) = \frac{u_*}{\kappa}\ln[(z-d)/z_0] \tag{3}$$

where $\kappa = 0.4$. This gives $z_0 = 3.8$ mm. The measured profile is coincident with the logarithmic profile in the range $1.7 < z/h < 3.7$, demonstrating again how the inertial sublayer is squeezed between the roughness sublayer and the outer layer.

Our values of z_0 and d differ from values previously measured over this surface by Brunet *et al.* (1994), who found d = 33 mm = $0.71h$ and z_0 = 5.6 mm. However, these were measured at a lower wind speed (by about 20%). Since the Reynolds number of the stalks of the model wheat (based on stalk diameter and mean wind speed) is 60 at the top of the canopy and much less lower down, we anticipate a significant wind speed dependence of the stalk drag coefficient and therefore of bulk momentum transfer properties such as z_0 and d.

3. Mean Velocity Fields

To facilitate comparisons between different configurations, a single scaling factor was applied to the velocities measured in each configuration. This scaled the velocities (as nearly as possible) to those that would have been observed under identical external conditions. For a particular configuration, the chosen scaling factor was the ratio of $\langle \bar{U}(z = 2H) \rangle_x$ in that configuration (where $\langle \ \rangle_x$ denotes a streamwise average) to $\bar{U}(z = 2H)$ for the undisturbed profile. This scaling factor was very close to 1 except for the M12H configuration. For M12H, the scaling factor was 1.34 because the adjustable roof was higher than for other configurations, resulting in lower free stream wind speeds.

The following subsections discuss three views of the mean velocity field $\bar{U}(x, z)$, respectively from vertical profiles at a sequence of x-stations, streamwise transects at a sequence of heights, and mean streamlines. Each view illuminates different facets of the flow. In each subsection we include data from the high-intensity turbulence regions near the windbreak, even though these data are more likely to be affected by triple-probe errors (Section 2.2) than data from elsewhere. Two pieces of evidence suggest that the data from near the break are sufficiently reliable to be useful. First, the absence of recirculation zones in any configuration, according to tests with woollen tufts (Section 2.2). Second, the triple-probe velocity measurements in the bleed flow ($x/H = +0.1$) agree well with the bleed flow velocity inferred from the measured static pressure drop across the windbreak and the pressure coefficient (further details will appear in a subsequent paper discussing pressure fields and momentum budgets).

3.1. VERTICAL PROFILES

Figure 5 shows vertical profiles of $\bar{U}(x, z)$ at a sequence of x-stations, for each of the five windbreak configurations. Profiles for the three single break configurations (Sld, Smd, Shd) were recorded at $x/H = -2, -1, +0.1, 1, 2, 3, 5, 8, 12$, whereas those for multiple configurations (M12H, M6H) cover one complete "cell" of the regular windbreak array. Continuity demands that both $\bar{U}(x, z)$ and $\bar{W}(x, z)$ are continuous through the break, so values of $\bar{U}$ measured just downwind of the break (at $x/H = +0.1$) are likely to be very similar to values just upwind (say

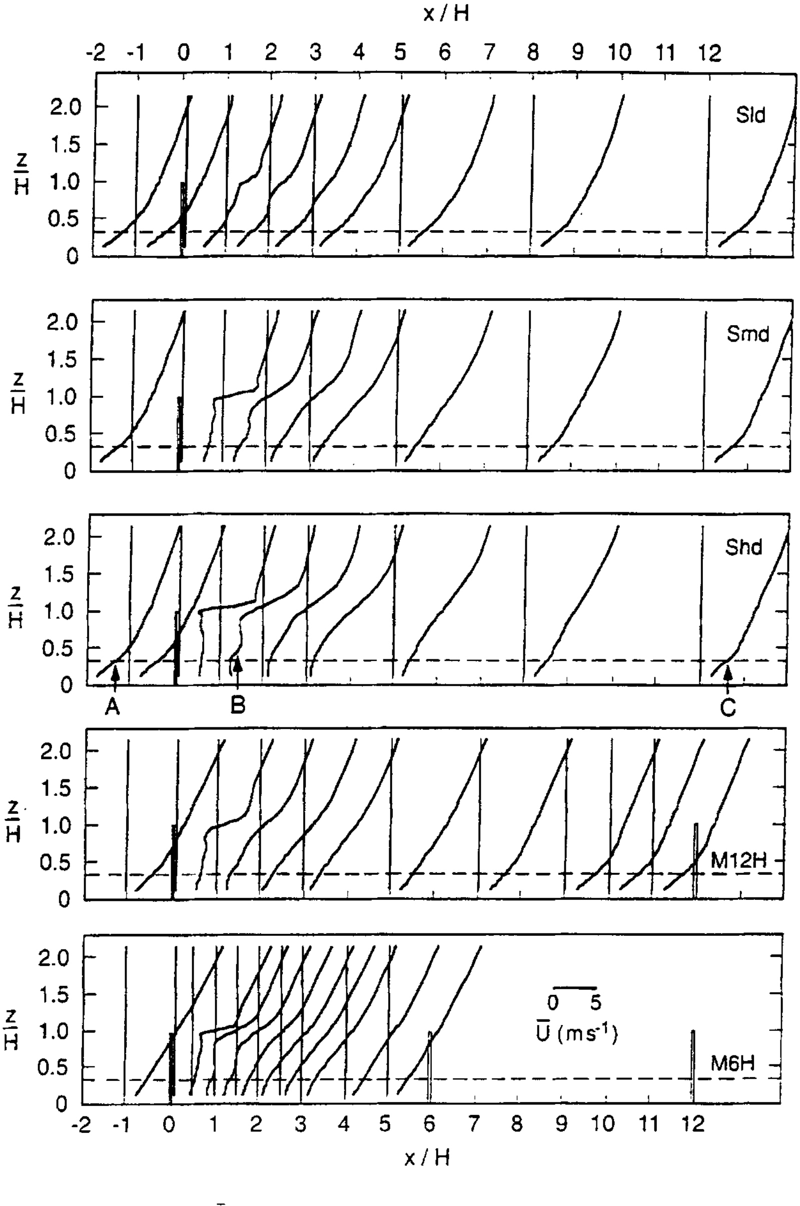

Figure 5. Vertical profiles of $\bar{U}(x, z)$, for configurations Sld, Smd, Shd, M6H, and M12H. The velocity scale is shown on the figure. Vertical lines denote both the wind speed origin for each profile and its location in the x direction. The horizontal dashed line denotes the canopy height $z = h$. Points A, B, C are inflection points discussed in text.

$x/H = -0.1$) which could not be measured. Profiles at $x/H = -1$ for Smd are missing, owing to an erroneous data set.

Three features are significant. First, a strong shear layer forms immediately downstream of the top of the windbreak. This layer is identified by a point of inflection in $\bar{U}(z)$, high values of the mean shear $\partial\bar{U}/\partial z$, and also by high values of the Reynolds stresses (see later). The mean shear increases with solidity (Sld to Shd) but is reduced in the multiple configurations, in comparison with a single break of the same solidity (Smd). The shear layer spreads vertically as it is carried downstream, contacting the canopy at $x/H \approx 3$ (this is clearest in the profiles of Reynolds stresses shown later). As argued in more detail later, the properties of this strong shear layer are characteristic of the classical mixing layer formed between two uniform, coflowing streams. Therefore, from here on, we use the term "mixing layer" for this shear layer, and refer to the associated flow region (Figure 1) as the mixing zone.

A second feature of Figure 5 is that the mean shear $\partial\bar{U}/\partial z$ in the bleed flow through the windbreak (measured at $x/H = +0.1$) is small. The bleed flow shear decreases as solidity increases, to the point where there is essentially no shear (in fact, a slightly negative $\partial\bar{U}/\partial z$) immediately behind the densest break (Shd). The absence of shear in the bleed flow just downwind of the break extends into the canopy as well as above it. Since the bleed flow is related by Equation (1) to the pressure drop ΔP across the break, ΔP also becomes less dependent on height as k increases. These trends are consistent with the observation of Laws and Livesey (1978) that as the solidity of a screen filling a pipe tends towards a pressure coefficient k of 2.8, the downstream flow tends towards radial uniformity, independent of the form of the approach profile.

The third feature is the sequence of events in the canopy as the flow moves downstream, most clearly evident for the dense break (Shd). The sequence starts in the approach flow, with its canopy shear layer and associated inflection in $\bar{U}(z)$ at $z = h$ (marked as A in Figure 5, but shown more clearly in Figure 4). The inflection is then obliterated as the flow passes through the break, in association with the near-zero $\partial\bar{U}/\partial z$ in the bleed flow. Next, the action of canopy drag causes a second canopy shear layer with an inflectional $\bar{U}(z)$ to develop in the near lee of the break (marked as B in Figure 5). This inflection is in turn obliterated at around $x/H \approx 3$, as the spreading mixing layer makes contact with the canopy; in this region the shear in the profile within and above the canopy is fairly uniform with height. Finally, a third canopy shear layer develops as the flow moves further downstream (marked as C in Figure 5), and a profile similar to the approach flow is eventually re-established. This sequence appears for all solidities, though less dramatically for configurations Smd and Sld.

3.2. STREAMWISE TRANSECTS

For each configuration, Figure 6 shows the mean velocity field in the form of streamwise transects $\bar{U}(x)$ at a sequence of 30 heights. To produce this figure, data at each x-station were interpolated vertically to give velocities at the 30 selected heights, but no horizontal smoothing was applied. The heights can be identified relative to the canopy (h) and windbreak (H) heights, for which the transects are highlighted. For clarity, the transects are represented by straight line-segments linking data from discrete x-stations, but this presentation should not be interpreted as if the data were continuous in x. In particular, data immediately around the windbreaks are fairly sparse, with data points only at $x/H = -1, +0.1$ and $+1$.

Upstream of the windbreak, three layers can be discerned, with different properties of the acceleration $\partial\bar{U}/\partial x$. (Note that the accelerations inferred from Figure 6 are actually streamwise averages, $\Delta U/\Delta x$, over the intervals Δx between successive x-stations. Also, we will speak of acceleration and deceleration along lines of constant height, though strictly these terms should be applied to velocity changes along streamlines; the following discussion remains true in either view.) First, above the windbreak height ($z > H$), the flow accelerates as it approaches the break and decelerates after passing over it, leading to a velocity maximum near the break. The most pronounced maxima in $\bar{U}(x)$ occur just above the break, with the peak located near the break in x; at greater heights, the x location of the maximum moves downstream. The magnitude of the maximum increases with solidity. In the second layer, covering the height range $h \lesssim z \lesssim H$, the flow decelerates as it approaches the windbreak. The lower boundary of this upwind decelerating layer extends closer to the ground with increasing solidity. In the third, lowest layer ($0 < z \lesssim h$), the flow again accelerates towards the break. The acceleration in this layer is marginally greater at higher solidities, but extends closer to the top of the canopy at lower solidities. The combination of deceleration above the canopy ($h \lesssim z \lesssim H$) and acceleration within ($0 < z \lesssim h$) leads to a profile of the bleed velocity through the break ($\bar{U}(0, z)$) which varies little with height, consistent with Figure 5. The height dependence of the bleed flow has already been shown to decrease with increasing solidity.

Immediately downstream of the windbreak the flow decelerates to a minimum in $\bar{U}$, at a streamwise position which varies with height in a complex manner. Throughout the canopy, and up to $z \approx 0.6H$, this minimum point occurs at $x/H \approx 2$–3. With increasing height, the minimum then moves rapidly closer to the windbreak (to $x/H \approx 0$ at $z \approx H$) and again moves downstream as z increases beyond H. This tendency is enhanced by solidity. Further downstream ($x/H \gtrsim 3$) there is a slow acceleration with x at all heights up to $z \approx 1.5H$. Above this height the flow tends to decelerate; both trends bring the flow back towards the approach profile.

Besides these features, the two multiple break configurations show lower scaled velocities near and below $z = H$, when compared with Smd (which has the same solidity). This is most evident in M6H, but is also discernible in M12H. There are two opposing effects at work here: first, the upwind breaks contribute to the large-scale roughness, leading to the development of a deep internal boundary layer over the entire windbreak ensemble in which the mean wind is reduced relative to that for a single windbreak. This internal boundary layer is basically similar to that forming over any smooth-to-rough transition (Kaimal and Finnigan, 1994). The effect of upwind breaks (beyond the one immediately upwind) can be thought

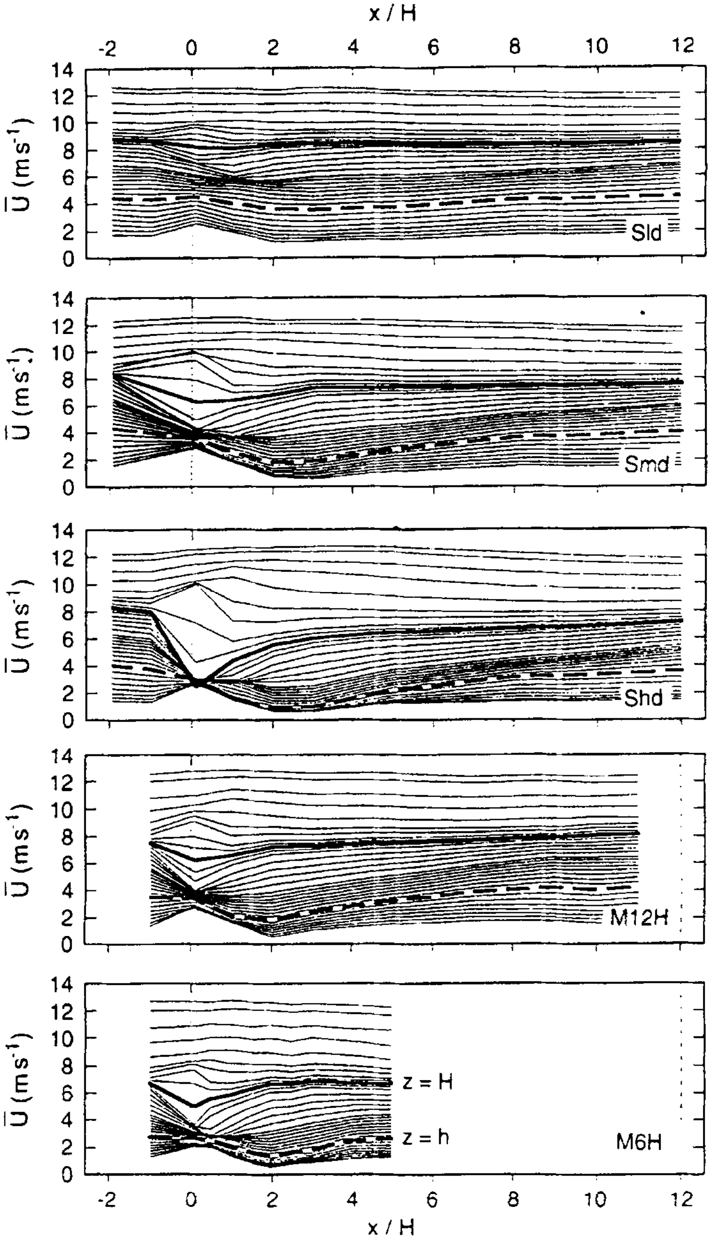

Figure 6. Streamwise profiles of $\bar{U}(x, z)$ at 30 heights, for all configurations. Heavy dashed line is the profile at canopy height ($z = h$); heavy solid line is the profile at windbreak height ($z = H$). Profiles are shown as straight line-segments linking data from $x/H = -2, -1, +0.1, 1, 2, 3, 5, 8$ and 12.

of as "nonlocal shelter". One of its properties can be seen in the far field of the multiple break configurations, which forms the approach flow for the following break. Whereas the flow associated with single breaks continues to accelerate downstream, wind speeds in the lower part of the profile begin to decrease after $x/H = 4$ for M6H, and $x/H = 9$ for M12H. Thus, the flow begins to decelerate $2H$ or $3H$ upwind of the next windbreak within the multiple arrays. The second (opposing) effect will be discussed in detail later: the rough-wall internal boundary layer over the multiple arrays induces higher turbulence levels, which transport momentum downward into the quiet zone more effectively than for the single breaks. This leads to a reduction in the shelter effect of any one member of a multiple array, relative to its isolated counterpart.

3.3. STREAMLINE PATTERNS

The (mean) stream function $\psi(z)$ is defined by:

$$\psi(x, z) = \int_0^z \bar{U}(x, z)\,\mathrm{d}z \tag{4}$$

and carries complete information about $\bar{U}(x, z)$, albeit in a modified form. Mean streamlines are lines of constant ψ in the xz plane, or lines beneath which the mean streamwise mass flow is constant. Streamline convergence and divergence denote areas of acceleration and deceleration, respectively. Figure 7 shows the mean streamlines for the velocity fields for all configurations. The main feature is the pronounced "hump", or upward displacement of the streamlines in the sheltered region. The "most displaced streamline", the line undergoing the greatest upward displacement from far upwind to the peak of the hump, indicates the height below which there is the greatest reduction of height-integrated wind speed (Equation (4)) in the sheltered region. This streamline passes through the windbreak at a height of about $0.4H$ for all configurations, and is displaced upward to about $0.5H$ for Sld, $0.6H$ for the medium-solidity breaks (Smd, M6H, M12H), and $0.75H$ for Shd. On the most displaced streamline, the peak occurs at $x/H \approx 2.5$ for the single breaks, and $x/H \approx 1.8$ for the multiple configurations. However, the peak does not occur at the same x/H for all streamlines, moving toward the break with increasing height.

Upwind of the break, low-level streamlines (below the most displaced streamline) actually move downwards as they approach the break, corresponding with the upwind acceleration close to the ground noted in Figure 6. Far downwind in the single-break configurations, the top ($z \approx 2.5H$) streamlines recover to be approximately horizontal at $x/H \approx 6$, but are displaced upwards by about $0.15H$ for Shd (less for Smd and Sld). Lower streamlines continue to slope downwards, implying acceleration (at least below these streamlines) even at the furthest downstream station. The multiple configurations show less perturbation at the top levels, with

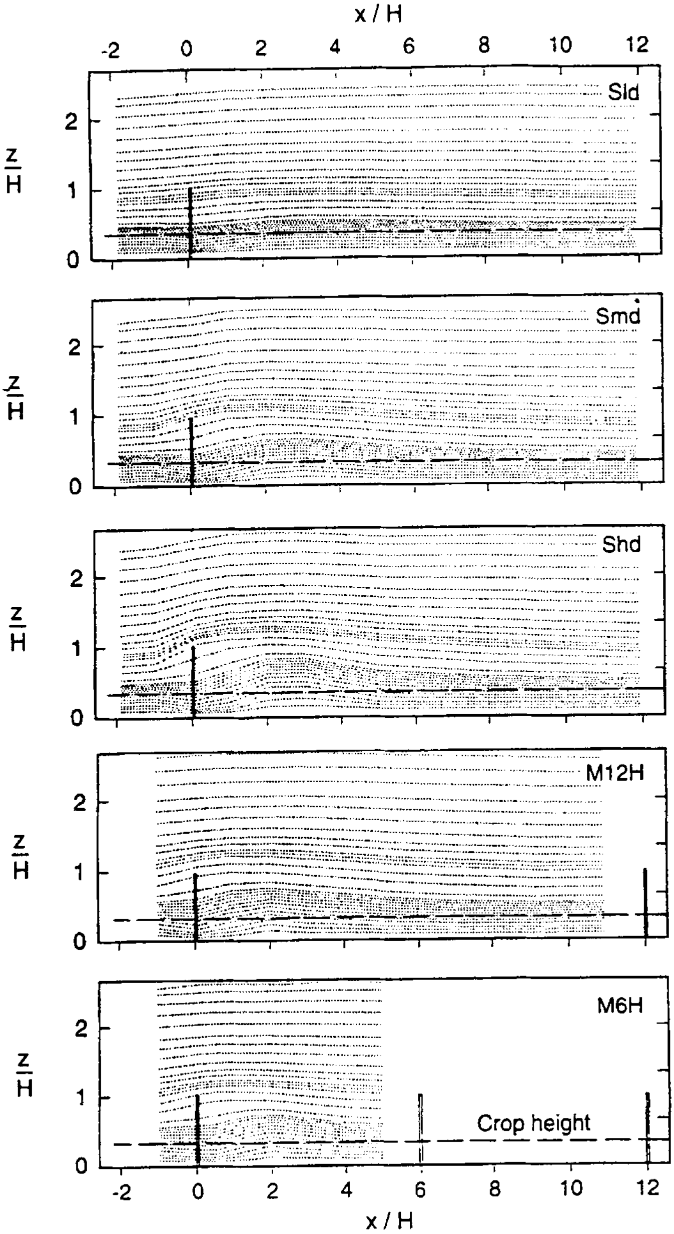

Figure 7. Mean streamlines for all configurations.

streamlines returning to close to their approach flow values ($x/H = -1$) by the equivalent position before the next windbreak.

4. Reynolds Stress Fields

Figures 8, 9 and 10 show vertical profiles of the velocity variances ($\overline{u^2}$, $\overline{w^2}$, $\overline{uw}$) for each configuration, at the same x-stations as the mean velocity field described above. Again our description follows the flow from upstream through the windbreaks. Upstream of the single windbreaks, the profile is very similar to the background profile (Figure 4), whereas the profiles associated with the multiple windbreaks reflect additional influences from upwind breaks. In these cases there is more overall curvature in the profiles and a less sharply defined interface at the canopy surface.

Downstream of the top of the windbreak, in the mixing zone, there is a prominent "nose" in the $\overline{u^2}$ and $\overline{uw}$ profiles. This is less pronounced, and develops later, in the $\overline{w^2}$ profile. In interpreting this observation, we must be wary of high-frequency measurement limitations at $x/H = 0.1$. Here the mixing layer is only a few millimetres deep, comparable to the averaging volume of the triple probe, so $\overline{uw}$ and $\overline{w^2}$ (and to a lesser extent $\overline{u^2}$) data are spectrally degraded by high-frequency and high-wavenumber losses (Section 2.2). However, allowing for this problem at $x/H = 0.1$, the trend of the observations at greater x/H indicates a physical mechanism. This can be seen from the production terms in the second moment budget equations (Kaimal and Finnigan, 1994).

Writing only the largest production terms explicitly, the budget equations for $\overline{u^2}$ and $\overline{uw}$ are:

$$\frac{\partial \overline{u^2}}{\partial t} = -\overline{uw}\frac{\partial \bar{U}}{\partial z} + \text{advection terms} + \text{turbulent transport} + \text{pressure terms}, \quad (5)$$

$$\frac{\partial \overline{uw}}{\partial t} = -\overline{w^2}\frac{\partial \bar{U}}{\partial z} + \text{advection terms} + \text{turbulent transport} + \text{pressure terms}. \quad (6)$$

In the mixing layer just downstream of the top of the break, $\partial \bar{U}/\partial z$ is large and both $\overline{uw}$ and $\overline{w^2}$ are of order $\overline{u^2}$ (just as in the approach flow). Consequently, there is strong production of both these Reynolds stress components. By contrast, the equation for $\overline{w^2}$ is:

$$\frac{\partial \overline{w^2}}{\partial t} = -\overline{uw}\frac{\partial \bar{W}}{\partial x} - \overline{w^2}\frac{\partial \bar{W}}{\partial z} + \text{advection terms} + \text{turbulent transport} \quad (7)$$
$$+ \text{pressure terms}.$$

Since both $\partial \bar{W}/\partial x$ and $\partial \bar{W}/\partial z$ are much smaller than $\partial \bar{U}/\partial z$, which appeared in the production terms for $\overline{u^2}$ and $\overline{uw}$, there is no comparable production of $\overline{w^2}$. The primary mechanism for increase in $\overline{w^2}$ is by redistribution of energy from $\overline{u^2}$, via the pressure-strain interaction terms in the second velocity moment budget equation. This process not only requires a prior increase in $\overline{u^2}$, but also acts on a

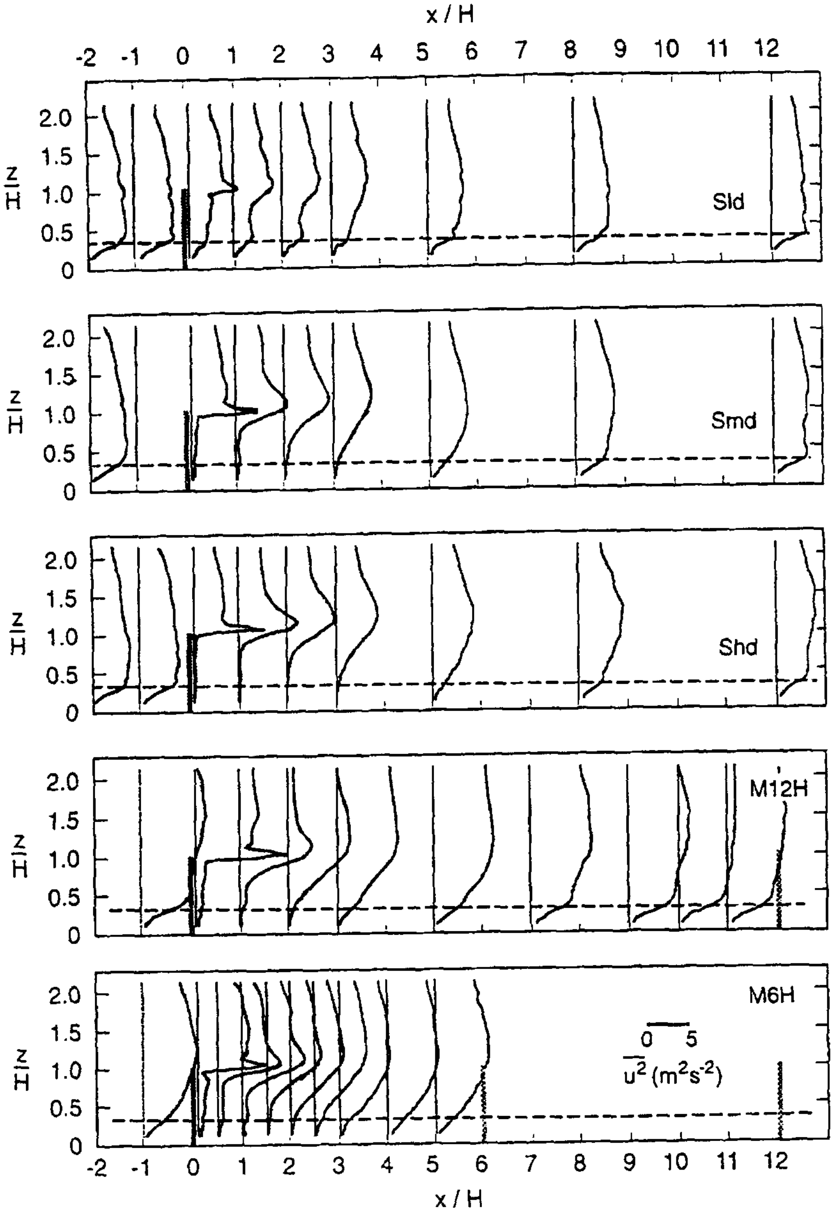

Figure 8. Vertical profiles of $\overline{u^2}$ for all configurations, plotted as in Figure 5.

time scale of the order of the turbulence time scale; consequently, increases in $\overline{w^2}$ only appear further downstream, at $x/H \gtrsim 1$.

A complementary, more picturesque, argument is that $\overline{u^2}$ variance (but not $\overline{w^2}$) is created by the random movement of a thin, intense shear layer past a stationary probe just downwind of the top of the break, under the action of the large-scale

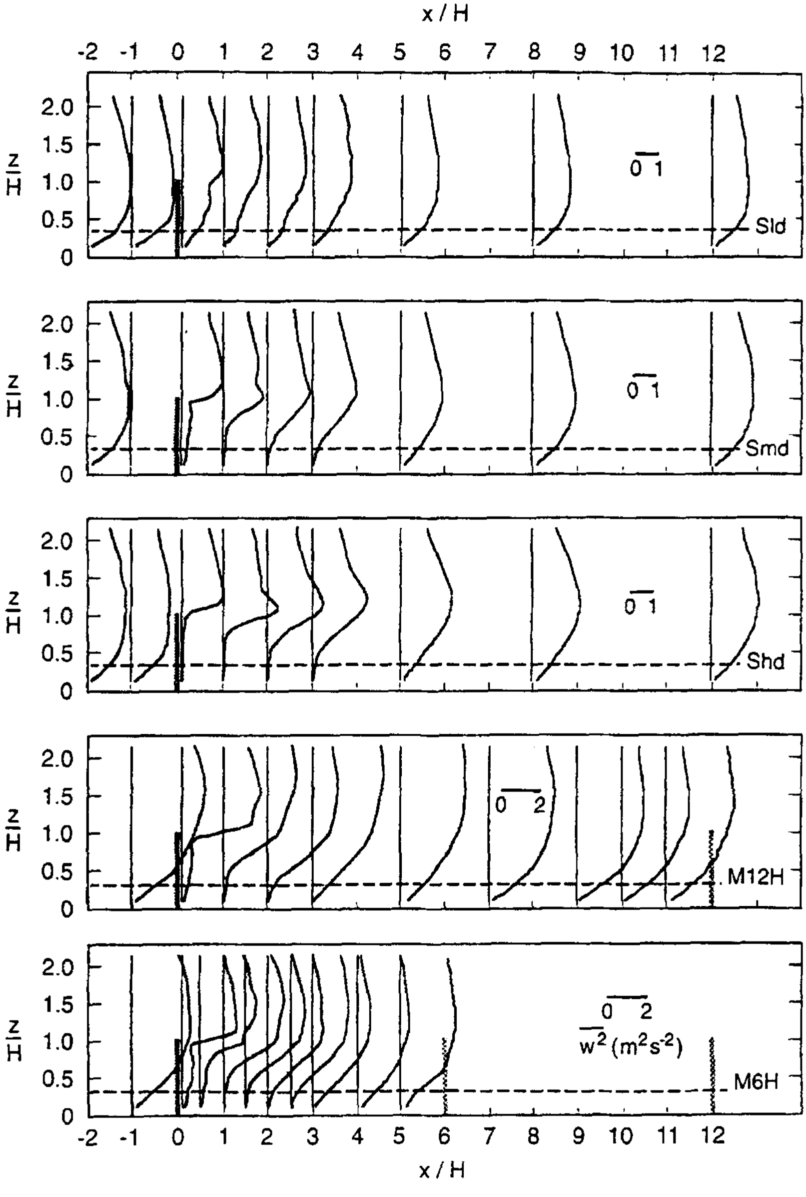

Figure 9. Vertical profiles of $\overline{w^2}$ for all configurations, plotted as in Figure 5.

upstream turbulence. This process also generates significant $\overline{uw}$, because downward moving air ($w < 0$) correlates strongly with faster than average U ($u > 0$), and *vice versa*.

In the bleed flow just downstream of the windbreak, all Reynolds stress components are substantially reduced below their upwind values, with greater reductions

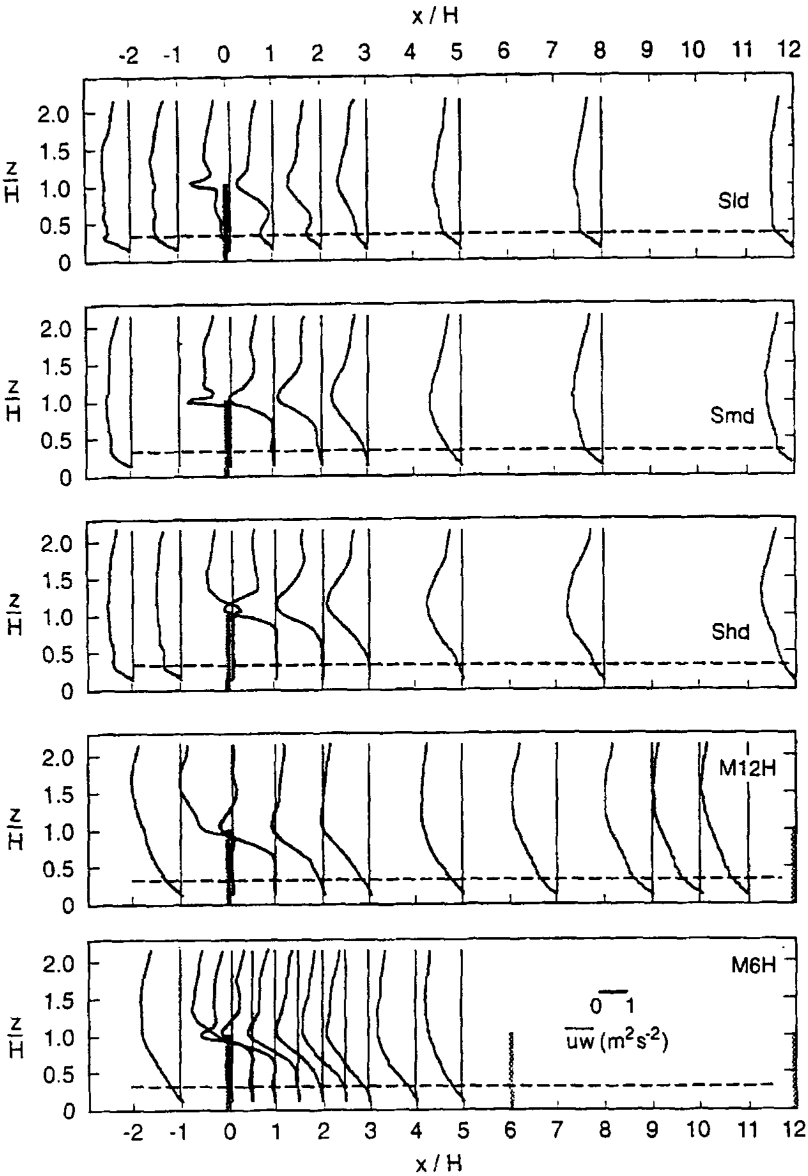

Figure 10. Vertical profiles of $\overline{uw}$ for all configurations, plotted as in Figure 5.

associated with increasing solidity. For Shd, Reynolds stresses are practically eliminated from the bleed flow. The (very small) remaining $\overline{uw}$ in the Shd bleed flow is actually positive, in accord with the negative $\partial\bar{U}/\partial z$ in this position.

Moving further downwind of the break ($x/H \gtrsim 1$), the evolution of all the profiles is quickly dominated by the vertically spreading mixing layer. At the centre height of this layer (initially $z = H$), the peak Reynolds stresses attenuate downstream, whereas the regions above and below this peak "import" Reynolds stresses by outward diffusion from the core of the mixing layer, causing a temporary stress increase in these regions. The increased stresses contact the canopy at $x/H \approx 3$, consistent with similar contact for $\bar{U}$ (Figure 5). However, this contact does not cause a dramatic surge in any of the measured Reynolds stress components at the top of the canopy, consistent with field results from Bradley and Mulhearn (1983).

Finally, the increased stresses are dissipated yet further downstream, and the stress profiles return to those in the approach flow (for the single break configurations). In line with the arguments above, the peaks in $\overline{u^2}$ and $\overline{uw}$ remain larger than the $\overline{w^2}$ peak throughout, and persist further downstream. The heights of the $\overline{u^2}$ and $\overline{uw}$ peaks initially rise and subsequently fall slowly, broadly following the streamline pattern in Figure 7 (Finnigan and Bradley, 1983). This trend is not clear for the weaker and later-formed $\overline{w^2}$ peak. The vertical spread of the region of excess stress is similar for all three components.

5. Scaling of Windbreak Flow

5.1. DIMENSIONAL ANALYSIS

The literature review in the introduction, and the results presented so far, suggest that windbreak flows are governed by a few controlling physical parameters. For a mean wind normal to a long single windbreak over a uniform rough surface, these parameters are windbreak height H, roughness length z_0 of the underlying canopy, solidity σ, and a measure of the incident wind speed which we take to be U_H, the background wind speed at height H. Additional parameters for a multiple windbreak array are the streamwise spacing ΔX and perhaps the overall fetch X_f over the multiple array. Two other parameters are not varied in these experiments: the Monin–Obukhov length L (irrelevant when $|H/L|$ is small), and the boundary layer depth δ (irrelevant when H/δ is small). In these experiments, $H/L = 0$ because the wind tunnel flow is thermally neutral, and H/δ is about 0.26 (see earlier discussion).

It follows that velocity moments are functions of position (x, z) and the parameters U_H, H, z_0, σ, and also ΔX and X_f for multiple arrays. In dimensionless form, the mean wind field can be written as

$$\frac{U(x,z)}{U_H} = F_U(x/H, z/H, z_0/H, \sigma; \Delta X/H, X_f/H), \tag{8}$$

with the parameters to the right of the semicolon important for multiple arrays only. Similar relationships, involving dimensionless functions F_{uu}, F_{ww} and F_{uw}, can be written for the Reynolds stress components $\overline{u^2}$, $\overline{w^2}$ and $\overline{uw}$.

Clearly, dimensionless functions of four variables (more in the multiple case) are not practical to quantify. However, significant simplifications exist within some zones of the windbreak flow identified in Figure 1. For instance, the only parameters relevant in the approach flow (where conventional surface-layer similarity theory applies) are U_H, z and z_0. In the bleed flow, it is likely that U_H and σ are the dominant parameters. In the following we analyse in particular the scaling properties of the mixing zone, following suggestions from previous work (Plate, 1971b; Wang *et al.,* 1990; Zhuang and Wilson, 1994) that the windbreak mixing layer has many properties in common with the classical mixing layer.

5.2. MIXING LAYER SCALING

The "classical" turbulent mixing layer is the shear layer formed between two uniform, nonturbulent, unbounded, coflowing streams of different streamwise velocities (say U_0 and U_1, with $U_0 < U_1$) which are allowed to mix across a plane z = constant (e.g. Wygnanski and Fiedler, 1970; Townsend, 1976; Rogers and Moser, 1994). Consistent with our experimental configuration, x and z are the streamwise and cross-stream (vertical) coordinates, respectively. The flow, which has a single point of inflection in the $\bar{U}(z)$ profile, quickly becomes turbulent and then self-similar after initiation. In general, self-similarity means that there exist length and velocity scales $L_s(x)$ and $U_s(x)$, and a height origin $Z_s(x)$, such that

$$\frac{\bar{U}(x,z)}{U_s(x)} = f_U(\zeta), \quad \frac{\overline{u^2}(x,z)}{U_s^2(x)} = f_{uu}(\zeta),$$
$$\frac{\overline{uw}(x,z)}{U_s^2(x)} = f_{uw}(\zeta), \quad \frac{\overline{w^2}(x,z)}{U_s^2(x)} = f_{ww}(\zeta), \tag{9}$$

where

$$\zeta = \frac{z - Z_s(x)}{L_s(x)}, \tag{10}$$

so that the velocity and Reynolds stress profiles collapse to dimensionless functions independent of streamwise position.

In the case of the classical mixing layer once self-similarity is achieved, the length scale L_s grows linearly with x, so the growth rate $\mathrm{d}L_s/\mathrm{d}x$ is constant for a given mixing layer. For later purposes, it is convenient to define L_s as the depth of the mixing layer, specified by the points at which $\overline{uw}(z)$ falls to 1% of its maximum value. This can be related to a more common mixing-layer length scale, the "vorticity thickness" $\delta_\omega = (U_1 - U_0)/(\mathrm{d}U/\mathrm{d}z)_{\mathrm{max}}$, by $L_s = 1.56\delta_\omega$ (from data in Rogers and Moser, 1994). The growth rate $\mathrm{d}L_s/\mathrm{d}x = 1.56\ \mathrm{d}\delta_\omega/\mathrm{d}x$ depends on the "velocity ratio" $\Delta U/U_{av}$, the ratio of the velocity difference $\Delta U = U_1 - U_0$ and the average velocity $U_{av} = (U_1 + U_0)/2$, such that the normalised growth rate $r_\omega = (U_{av}/\Delta U)\,\mathrm{d}\delta_\omega/\mathrm{d}x$ is approximately constant. Observations reviewed by Rogers and Moser (1994) give $r_\omega = 0.09 \pm 0.01$. It follows that

$$(\mathrm{d}L_s/\mathrm{d}x)_{\mathrm{class}} = (L_s/\delta_\omega) r_\omega \Delta U/U_{av} = 0.14\Delta U/U_{av}. \tag{11}$$

The velocity scale $U_s(x)$ for the classical mixing layer is ΔU, which is x-independent. The z origin $Z_s(x)$ is usually chosen as the locus of points where $\bar{U}(z) = U_{av}$. The data of Wygnanski and Fiedler (1970) show that the mean flow is very nearly antisymmetric about the centreline $z = Z_s(x)$, with the $\bar{U}$ inflection point close to this line. The profiles of $\overline{u^2}$ and $\overline{uw}$ are symmetric, but the peak in $\overline{w^2}$ lies slightly on the high velocity side of $Z_s(x)$. Along the centreline, the turbulence is characterised by normalised standard deviations σ_u/u_*, σ_v/u_* and σ_w/u_* of 1.80, 1.54 and 1.43, respectively, and hence $\sigma_u/\sigma_w = 1.26$ (here u_* is defined from the peak $\overline{uw}$). By contrast, the same quantities in a surface boundary layer (without windbreaks) are typically 2.5, 1.8 and 1.25, with $\sigma_u/\sigma_w = 2.0$ (Panofsky and Dutton, 1984).

The classical mixing layer may be compared with the windbreak mixing layer in our experiments. The obvious gross similarity is the inflectional $\bar{U}(z)$, while the obvious difference is that the windbreak mixing layer exists in an environment of strong, vertically inhomogeneous, large-scale background turbulence, unlike the classical mixing layer for which the mixing streams are uniform and nonturbulent. More detailed comparison can be made on several points. First, for the windbreak mixing layer, the locus of the $\bar{U}(z)$ inflection reduces in height downstream of the windbreaks, whereas the peaks in the Reynolds stress profiles (roughly) follow streamlines, slightly rising and then falling. The behaviour of the $\bar{U}(z)$ inflection is a result of the asymmetry of the windbreak flow, and the requirement that $\bar{U}(z)$ eventually returns to its background form; this occurs via a descent of the inflection point towards the ground before it is smoothed out (Figure 5). Second, we can examine the normalised standard deviations in the windbreak mixing layer. Figure 11 shows the streamwise evolution of $(\overline{u^2}/(-\overline{uw}))^{1/2}$ at $z/H = 1$ (this quantity is used instead of σ_u/u_* because $\overline{uw}$ varies strongly with position; the line $z/H = 1$ is used as a simple surrogate for the locus of the peak in $\overline{u^2}$, or $Z_s(x)$). For the single break configurations, this quantity falls from values typical of a surface-layer (2.3–2.5), observed upstream of the break, to values typical of a classical mixing layer (around 1.8) at $x/H \approx 2$; it finally rises slowly back towards surface-layer values with further increase in x/H. For Sld the final values are close to those upstream, whereas for Smd and Shd they remain lower. The two multiple configurations exhibit similar trends, with slightly different numerical values.

Against this background, we now test whether the windbreak mixing layer possesses the self-similarity properties of its classical counterpart; that is, whether the general scaling laws of Equation (8) reduce to Equations (9) and (10) in the mixing zone. To find the streamwise dependence of the scales $L_s(x)$ and $U_s(x)$ to within an arbitrary multiplicative factor, we construct empirical scales which graphically collapse the $\overline{uw}$ profiles, and then test how well these scales collapse other profiles. The choice of $\overline{uw}$ as the basis for graphical collapse is arbitrary; similar results are obtained with other choices. Figure 12 shows, for all configurations, scales $L_s(x)$ and $U_s(x)$ which collapse the $\overline{uw}$ profile around its central peak (taken to define Z_s). Figure 13 shows the resulting scaled $\bar{U}$,

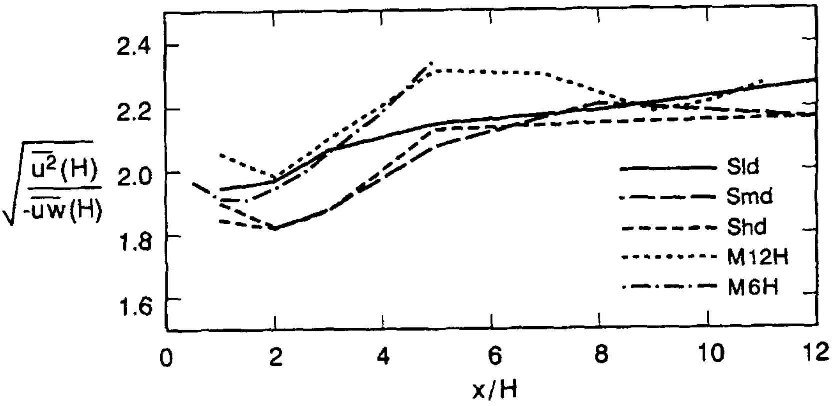

Figure 11. Streamwise evolution of $(\overline{u^2}/(-\overline{uw}))^{1/2}$ at $z/H = 1$, for all configurations.

$\overline{u^2}$, $\overline{w^2}$ and $\overline{uw}$ profiles, for the Shd configuration only (omitting the data from $x/H = 0.1$ because of the spectral degradation in $\overline{w^2}$ and $\overline{uw}$). The results for other configurations are similar. Scaling on the basis of visual graphical collapse enables us to estimate these empirical similarity scales over the complete downstream wind field (though we may not be able to interpret the scales in a mixing layer context in the far downwind region); by contrast, selecting characteristic points, such as points of maximum slope, on individual profiles is only possible close behind the windbreak. The absolute value of U_s is set so that the peak normalised $\overline{uw}$ is -1, and the absolute L_s is set so that the width of the normalised $\overline{uw}$ profile is 1.

For all configurations, the length scale $L_s(x)$ (Figure 12a) is nearly linear in x (with a slight offset) for $x/H \lesssim 3$, and approaches constancy further downstream ($x/H > 6$). The linear behaviour near the break is consistent with expected behaviour in a classical mixing layer, but the magnitude of the growth rate $\mathrm{d}L_s/\mathrm{d}x$ is much larger in the windbreak case. As shown in Table II, the observed growth rate $\mathrm{d}L_s/\mathrm{d}x$ in the near-break region ($x/H \lesssim 3$) is about 0.4 for Sld, Smd and Shd, and 0.44–0.52 for M6H and M12H; by comparison, the growth rates for classical mixing layers with corresponding values of $\Delta U/U_{av}$, calculated from Equation (11), range from 0.04 (Sld) to 0.16 (Shd).

A qualitative interpretation of this trend is that, just downwind of the top of the windbreak, a thin layer of strong shear is being flapped about by the large-scale background turbulence. The windbreak mixing layer grows through two mechanisms: entrainment into the thin shear layer, driven by the small-scale, local eddies in that layer which resemble those in a classical mixing layer; and the flapping process itself, driven by the large-scale ambient turbulence. This also suggests why observed growth rates are higher behind the multiple than the single windbreaks, since the ambient turbulence intensity is higher in the multiple case because of the deep, rough-wall internal boundary layer generated over the entire windbreak ensemble. A quantitative assessment can be obtained by assuming that

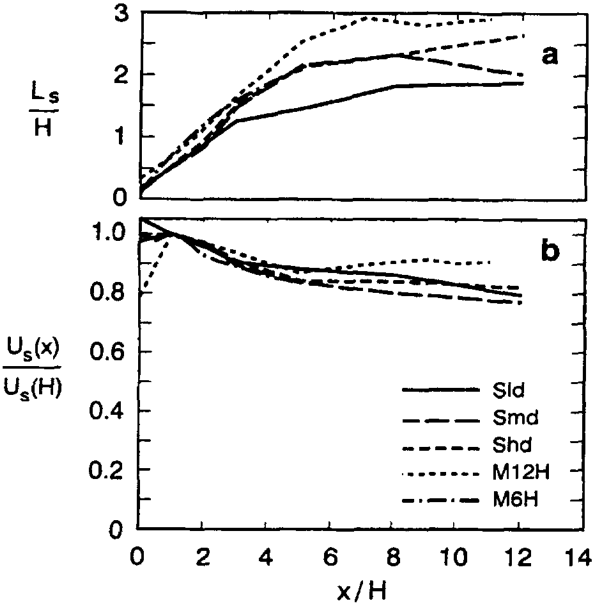

Figure 12. Graphically fitted (a) length scales $L_s(x)$, and (b) velocity scales $U_s(x)$ which collapse the $\overline{uw}$ profiles.

TABLE II
Predicted and observed growth rates $\mathrm{d}L_s/\mathrm{d}x$ in the windbreak mixing zone

	$\Delta U/U_{av}$	$(\mathrm{d}L_s/\mathrm{d}x)_{\text{class}}$ Equation (11)	σ_w/U $(z = H)$	$\mathrm{d}L_s/\mathrm{d}x$ Equation (12)	$\mathrm{d}L_s/\mathrm{d}x$ Observed
Sld	0.27	0.038	0.17	0.35	0.36
Smd	0.69	0.097	0.18	0.37	0.40
Shd	1.17	0.164	0.18	0.39	0.40
M12*H*	0.79	0.111	0.25	0.51	0.44
M6*H*	0.78	0.110	0.26	0.53	0.52

dispersive broadening of the windbreak mixing layer by the small-scale and large-scale processes can be added in root-mean-square fashion, as for superimposed random walks. This implies that:

$$\mathrm{d}L_s/\mathrm{d}x \approx \left[(\mathrm{d}L_s/\mathrm{d}x)^2_{\text{class}} + (2\sigma_w/U)^2_{\text{ambient}}\right]^{1/2}, \tag{12}$$

where the factor 2 appears in the ambient term because $x\sigma_w/U$ is an estimate of the half-depth of a near-field plume, whereas L_s is a measure of the full depth. Assuming that the local contribution to the growth rate is similar to that in a classical mixing layer, we take $(\mathrm{d}L_s/\mathrm{d}x)_{\text{class}}$ from Equation (11). To estimate the contribution to the growth rate due to the ambient turbulence, we use measured values for the ambient σ_w/U at $z = H$ (Table II). For each configuration, Table II

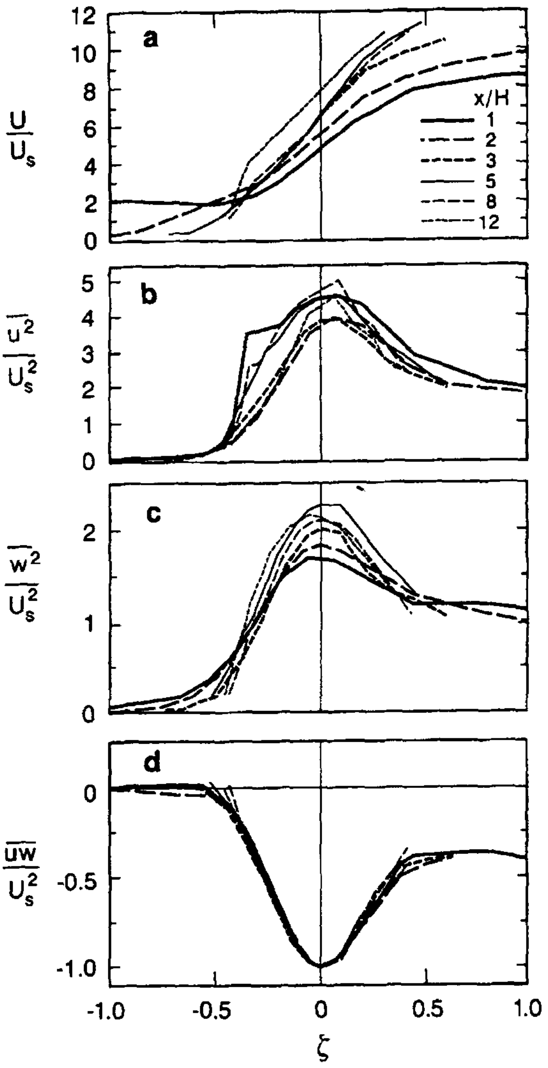

Figure 13. Collapse of the mean wind and Reynolds stress component profiles, using the scales L_s and U_s in Figure 12.

compares the prediction of Equation (12) with the observed values of $\mathrm{d}L_s/\mathrm{d}x$ in the near-break region ($x/H \lesssim 3$). The agreement is surprisingly good, considering the simplicity of Equation (12), suggesting that there is some validity to the view that the mixing zone consists of a thin, approximately classical mixing layer being flapped about by large-scale, ambient turbulence.

The velocity scale U_s (Figure 12b) reflects the observed trend in the magnitude of the peak in $\overline{uw}$ (Figure 10), showing a slow decrease (through about 15%) with increasing x/H. In contrast, the velocity scale for the classical mixing layer is

x-independent. A qualitative explanation for this difference is that the windbreak mixing layer exists in a strongly turbulent, sheared background flow in which the "driving" velocity difference ΔU diminishes with x because of the bleed flow and momentum diffusion into the quiet zone.

Regarding the shapes of the scaled profiles in Figure 13, the collapse for $\overline{uw}$ is excellent only because this quantity was used to define the scales L_s and U_s. The real test of mixing-layer similarity is the quality of the collapse for the other quantities. The collapse for $\overline{u^2}$ and $\overline{w^2}$, while not as good as for $\overline{uw}$, is quite good over the x/H range from 1 to 3 (after which the spreading mixing layer contacts the canopy) and remains reasonable even as far as $x/H = 8$. The collapse for $\bar{U}$ is degraded by three factors: a progressive displacement of the point of inflection from the ζ origin, associated with the decreasing trend in the height of the $\bar{U}$ inflection compared with the peaks in the Reynolds stress components in the windbreak mixing layer (noted above); the effect of the background shear well above the windbreak, which causes a steady increase in the scaled shear with x/H on the high-velocity side; and the contact of the spreading mixing layer with the ground.

Our results on mixing layer scaling can be compared with those of Castro and Haque (1987, 1988) who examined the relevance of this scaling for the separated flow behind a solid bluff plate at the leading edge of a splitter plate in both non-turbulent and turbulent free streams. They found that mixing layer scaling describes some aspects of the velocity field, but that its applicability diminishes with increasing x. They also found that free stream turbulence increased the spread rate of the strongly sheared layer and decreased the distance to the reattachment point. Our work, and Equation (12), are broadly consistent with this.

5.3. MOMENTUM TRANSFER ACROSS THE MIXING ZONE

Examination of the turbulent momentum exchange coefficient $K_m = -\overline{uw}(\partial\bar{U}/\partial z)^{-1}$ across the mixing zone provides another view of the momentum transfer processes behind a windbreak. Figure 14 shows the sequence of vertical profiles of K_m for the Shd configuration (with slight smoothing by eye). Again we follow the sequence downwind, taking as a comparison value the surface-layer similarity form $K_* = \kappa u_*(z - d)$, in the inertial sublayer above the canopy in the background flow (the straight line in Figure 14). In the undisturbed flow (represented here by the far-downwind profile at $x/H = 12$), K_m exceeds K_* in the canopy and roughness sublayers within and just above the canopy; $K_m \approx K_*$ in the inertial sublayer; and K_m is approximately constant with height in the outer layer. This behaviour is familiar from previous wind tunnel simulations of rough-wall boundary layers and canopy flows (Raupach *et al.*, 1980, 1986). Just downwind of the break K_m is severely reduced, to an extent depending on solidity (see Figure 15, discussed below). In the near-break region $x/H \lesssim 3$, there is a discernible zone around $z = H$ in which the K_m profiles show a tendency toward (but do not reach) constancy with height. This is the signature (in K_m) of the windbreak mixing layer,

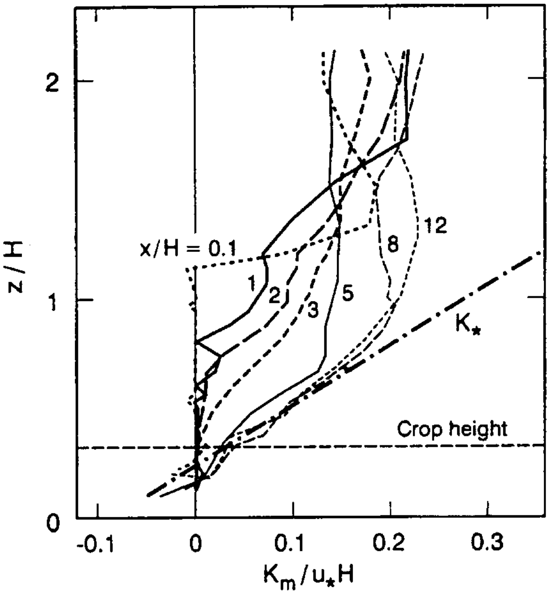

Figure 14. Vertical profiles of K_m for the Shd configuration.

but it is far narrower than the turbulence signature in the second-moment profiles used to define the length scale L_s. The effects of ambient turbulence are therefore strongly evident in the vertical structure of K_m. With further progress downwind, the K_m profiles re-equilibrate towards the background state.

Figure 15 shows, for all configurations, the streamwise variation of K_m at height $z = H$ (that is, approximately along the mixing-layer centreline). Anticipated features are the initially roughly linear increase of K_m with x in the mixing layer near the break, eventually followed by approach to a constant background value. The initial rate of increase is again linked to background turbulence and overall roughness, with the fastest rate of increase associated with the greatest roughness (M6H). The observed values of K_m in the core of the windbreak mixing layer (Figure 15) can be compared with values expected in a classical mixing layer, as follows. Wygnanski and Fiedler (1970, their Figure 40) found that K_m was approximately constant across the depth of their laboratory mixing layer, as modelled by Schlichting (1968): $K_m/(\Delta U x) = 0.002$. For our purpose it is convenient to use the velocity scale $(\sigma_w)_{\text{max}}$ rather than ΔU, since the maximum σ_w is better defined and less variable in the windbreak mixing layer. Wygnanski and Fiedler observed $(\sigma_w)_{\text{max}}/\Delta U = 0.138$ (independent of x); therefore, $K_m = 0.0145(\sigma_w)_{\text{max}} x$ in their laboratory mixing layer. Straight lines $K_m = 0.0145(\sigma_w)_{\text{max}} x$ are marked in Figure 15 for each configuration, using average values of $(\sigma_w)_{\text{max}}$ along the line $z = H$ for $0 < x/H < 3$. The observed K_m is typically larger than (around twice) the value expected in a classical mixing layer, consistent with the finding for the length scale L_s in the last section.

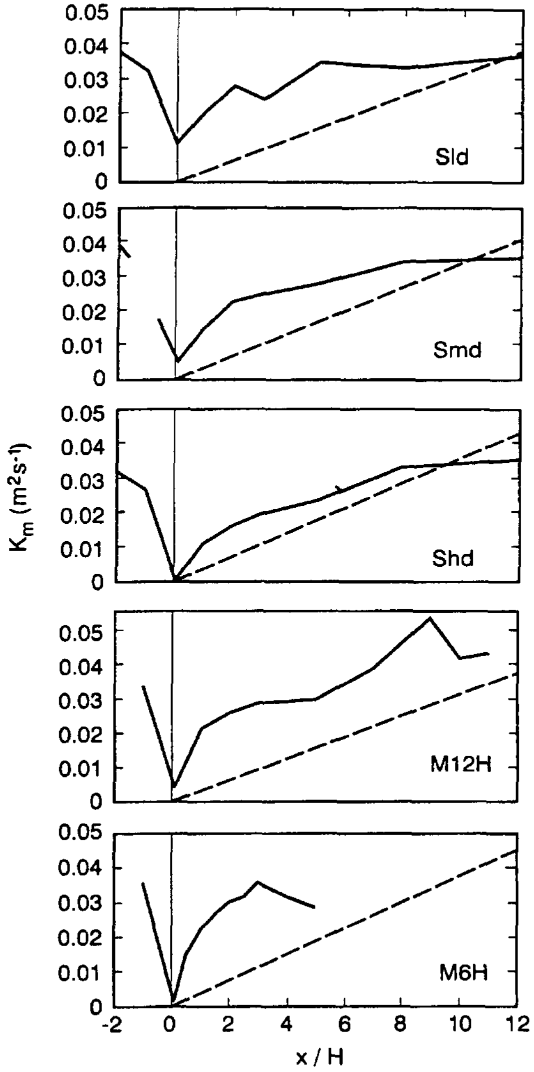

Figure 15. Streamwise variation of K_m at height $z = H$, for all configurations. Sloping dashed lines indicate expected values in a classical mixing layer, $K_m = 0.0145(\sigma_w)_{\max}x$.

6. Shelter Effectiveness

Lastly, and in a different vein, we use our data to assess the effects of windbreak solidity and spacing on shelter effectiveness. Unfortunately there are no generally accepted, straightforward measures relating crop production with wind protection. Therefore, the concept of shelter effectiveness has been quantified in many ways depending on the application, using a variety of wind field parameters (e.g. Gandemer, 1981; Argent 1990). The simplest measures of shelter effectiveness define a sheltered zone in terms of a recovery fraction for the mean wind speed, such as the zone over which $\bar{U}(x,z)/\bar{U}(\text{background}, z) < 0.9$; or alternatively the lee wind speed may be integrated over a prespecified sheltered area. More sophisticated measures of shelter effectiveness attempt to incorporate the likelihood of particular events by using the wind speed probability density function $p(U)$, often parameterised in terms of a few velocity moments. It is usually assumed that $p(U)$ is Gaussian, and the sheltered zone defined as a zone of reduction of $\bar{U} + n\sigma_u$ to less than some fraction (say 0.9) of its background value. The choice of n depends on the weight accorded the velocity fluctuations (e.g. $n = 3$ for a Gaussian wind speed distribution and a desired 99% probability level).

Here we quantify the effectiveness of the wind tunnel model windbreaks in terms of velocity and turbulence deficits relative to the approach flow. As the wind tunnel did not allow measurements of the undisturbed approach flow far upstream, we assume that the approach flow is specified by the background profiles measured at the test windbreak position in the absence of windbreaks, and scaled as described earlier (using the streamwise average of the wind speed at $z = 2H$). These background profiles compare very closely with profiles measured upstream ($x/H = -2$) of the single windbreaks. However, outdoor measurements (McAneney and Judd, 1991) show some reduction of overhead wind speeds at $z = 2H$ above multiple windbreaks, so that scaling on the velocity at this height may cause our estimates for the shelter effectiveness of multiple windbreaks to be conservative.

Figures 16 and 17 show dimensionless deficits for $\bar{U}$ and σ_w relative to the background flow for each configuration. These ratios, or "shelter factors", are defined by

$$S_U(x,z) = \frac{\bar{U}(\text{background}, z) - \bar{U}(x,z)}{\bar{U}(\text{background}, z)} \tag{13}$$

and similarly for σ_w, defining $S_w(x,z)$. Note that S_U is similar to the speedup ratio in the theory of flow over low hills, but with opposite sign to produce a positive number in the sheltered zone. For the single breaks, the upwind velocity deficits S_U above break height (Figure 16) indicate close agreement between the approach and background profiles ($S_U \approx 0$), while the upwind S_U values below $z = H$ show that shelter increases both as the windbreak is approached and also as solidity increases. Upwind S_U values are positive for the two multiple configurations, reflecting lower mean wind speeds than in the background flow. Immediately behind the break the shelter effect is approximately constant down to canopy level and then decreases sharply, reflecting the acceleration relative to the approach flow within the canopy (see Section 3). Above the windbreak height there is also some acceleration, particularly with the high solidity windbreak. For $x/H > 3$ the maximum protection appears just above crop height, with the degree of protection increasing with solidity. The velocity deficit is still clearly visible

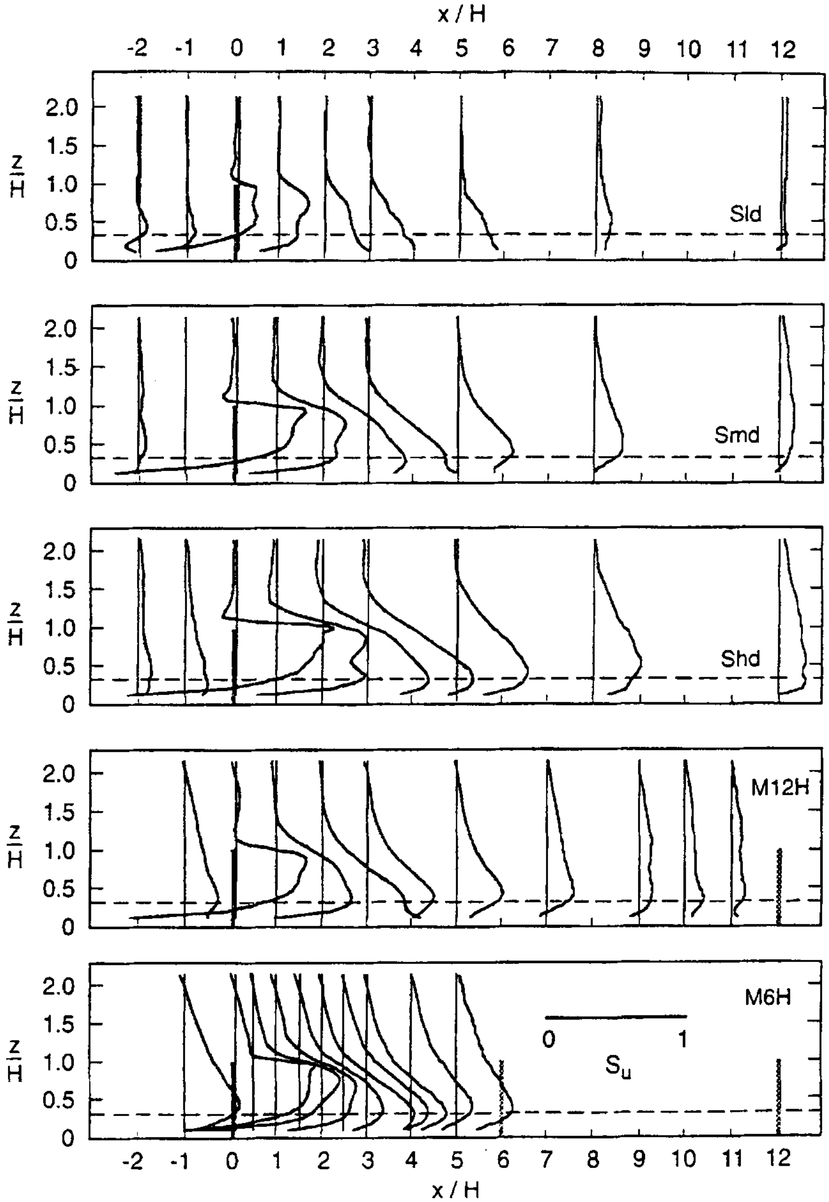

Figure 16. Relative velocity deficits $S_U(x, z)$ for each configuration.

at the most downstream position, again increasing with solidity. The deficit in the M6H configuration appears to recover cyclically to a very similar profile to that approaching the windbreak, whereas for M12H the deficit at $x/H = 11$ is considerably less than at $x/H = -1$, indicating that the internal boundary layer for M12H is further from equilibrium. If the profile at $x/H = -1$ is used in Equation

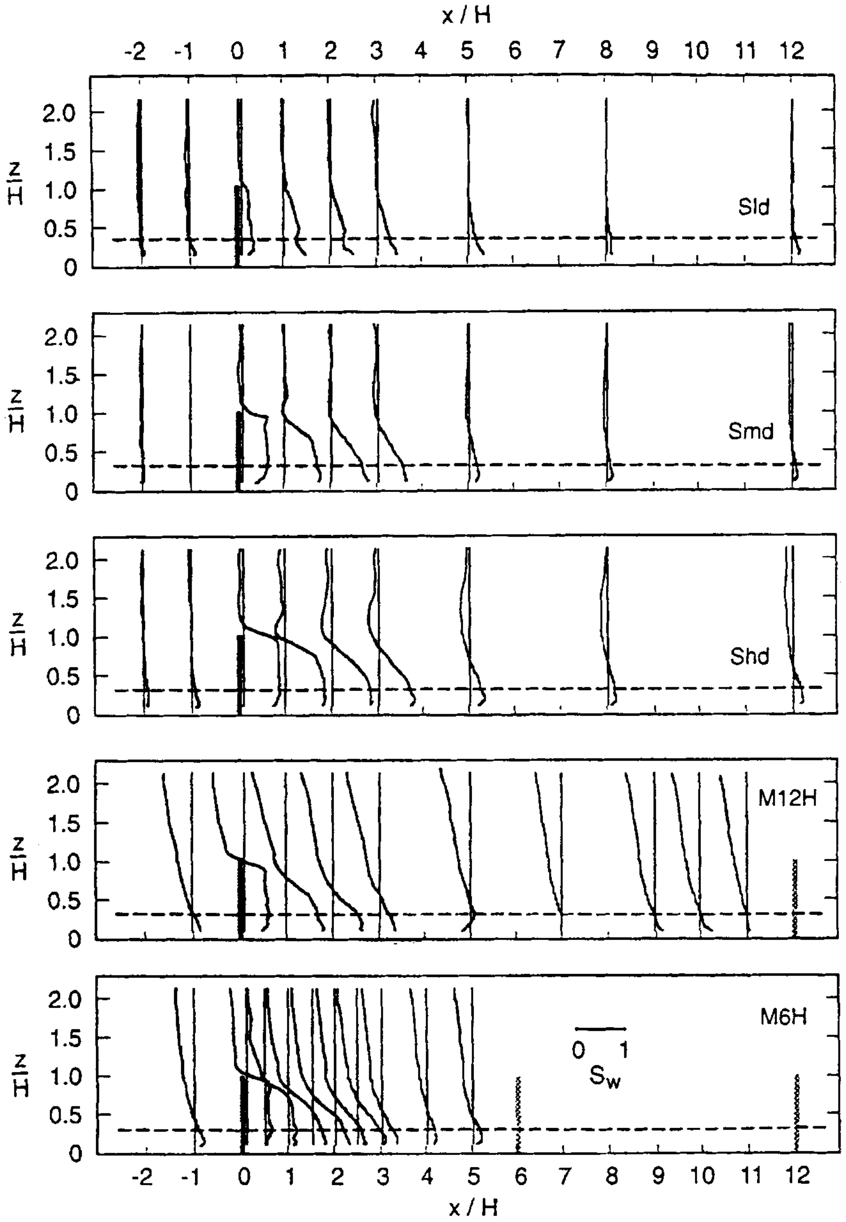

Figure 17. Relative σ_w deficits $S_w(x, z)$ for each configuration.

(13) as the background profile, then S_U for the multiple windbreaks is clearly less than for the single breaks, as has been observed in the field (profiles not shown).

Figure 17 shows similarly calculated σ_w deficits S_w. There is only a small upwind reduction in turbulence within the canopy, associated with the deceleration and streamline curvature in this region as for a canopy on a hill (Finnigan and

Brunet, 1995). Immediately downwind of the break, in the all-important canopy region S_w increases with solidity, but this effect is shortlived as there is little shelter effect within the canopy at $x/H = 5$. The recovery of turbulence is generally more rapid than that of mean wind speed, due to its production and diffusion in the mixing zone. Just above the canopy, this source of turbulence leads to negative values of S_w. The two multiple configurations clearly show the increased turbulence (relative to the background) above the windbreaks, caused by the increased overall roughness of the surface. Immediately in the lee of the windbreaks the deficit for the multiple breaks is similar to that for Smd, but this protection is again reduced downstream (e.g. at $x/H = 3, z/h = 1$) owing to the increased turbulence levels. For $x/H > 5$ some protection remains within the canopy, presumably resulting from less shear at canopy height owing to the lower overall wind speed.

7. Conclusions

The novel features of windbreak flows studied in this work concern the flow within the sheltered canopy, the properties of the mixing layer formed behind each windbreak, and the effects of multiple windbreaks. Each of these aspects is summarised separately.

A windbreak has some interesting effects on the flow within the sheltered canopy, both upwind and downwind of the break. There is an acceleration within the canopy just upwind of the break, in contrast with a deceleration above the canopy. This occurs because the overall pressure field is associated with a pressure difference across the break which (for the higher-solidity breaks) is practically independent of height, leading to a bleed flow which is similarly height-independent. This pressure difference drives the flow through the windbreak within the canopy at higher velocities than exist in the unsheltered canopy. Downwind of the break, the canopy flow decelerates to a velocity minimum (maximum shelter) near $x/H = 2.5$ in these experiments. Associated with this streamwise behaviour is an evolution in the mean velocity profile in the canopy, which in unsheltered conditions is marked by an inflection near the canopy top. This inflection is obliterated twice: once as the canopy flow passes through the break, and again at $x/H \approx 3$ when the spreading mixing layer meets the canopy. No dramatic surges in Reynolds stress components are observed at this point. This full range of features is observed at all windbreak solidities studied in these experiments; the perturbations from the approach flow increase with increasing solidity.

We have studied the flow and scaling properties of the windbreak mixing layer, comparing them with the classical mixing layer formed between two uniform coflowing streams of differing velocity. The windbreak mixing layer resembles its classical counterpart in possessing an inflectional $\bar{U}(z)$ profile, and in showing some characteristics of mixing-layer scaling in the near-break region before contact with the canopy ($x/H \lesssim 3$). In this region the similarity length scale L_s grows linearly with x (as in the classical mixing layer), but the growth rate $\mathrm{d}L_s/\mathrm{d}x$ in the near-break region ($x/H < 3$) is much larger in the windbreak mixing layer than in the classical case. We attribute this to the effects of background turbulence. This is also consistent with the finding that $\mathrm{d}L_s/\mathrm{d}x$ is larger for multiple than single windbreaks. Further downwind, mixing-layer similarity ceases to apply as the mixing zone begins to interact with the canopy. Finally, the flow is expected to revert to surface-layer similarity scaling at large x/H (larger than the maximum value $x/H = 12$ achieved in this experiment).

We have viewed a multiple windbreak array as additional upstream roughness, which generates an internal boundary layer characteristic of a smooth-to-rough transition. There are two main consequences of this: an overall decrease in wind speed due to the "nonlocal shelter" offered by upwind members of the multiple array; and an increase in ambient turbulence, leading to a decrease in the shelter efficiency of any one break in a multiple array relative to an equivalent single break (because the extra turbulence transports momentum more rapidly down into the quiet zone). Of these opposing effects, the former (nonlocal shelter) is dominant, leading to wind speeds within a multiple array that are smaller than those behind a single windbreak, given identical external conditions.

References

Argent, R. M.: 1990, 'Wind Shelter and Crop Protection', M. Eng. Sci. Thesis, University of Western Ontario, London, Ontario, Canada.

Baltaxe, R.: 1967, 'Airflow Patterns in the Lee of Model Windbreaks', *Arch. Meteorol. Geophys. Bioklimatol. Series B.* **15**, 287–312.

Bean, A., Alperi, R. W., and Federer, C. A.: 1975, 'A Method for Categorizing Shelterbelt Porosity', *Agric. Meteorol.* **14**, 417–429.

Bradley, E. F. and Mulhearn, P. J.: 1983, 'Development of Velocity and Shear Stress Distributions in the Wake of a Porous Shelter Fence', *J. Wind Eng. Ind. Aerodyn.* **15**, 145–156.

Brunet, Y., Finnigan, J. J., and Raupach, M. R.: 1994, 'A Wind Tunnel Study of Air Flow in Waving Wheat: Single Point Velocity Measurements', *Boundary-Layer Meteorol.* **70**, 95–132.

Castro, I. P.: 1971, 'Wake Characteristics of Two-Dimensional Perforated Plates Normal to an Air Stream', *J. Fluid Mech.* **46**, 599–609.

Castro, I. P. and Haque, A.: 1987, 'The Structure of a Turbulent Shear Layer Bounding a Separation Region', *J. Fluid Mech.* **179**, 439–468.

Castro, I. P. and Haque, A.: 1988, 'The Structure of a Shear Layer Bounding a Separation Region. Part 2. Effects of Free-Stream Turbulence', *J. Fluid Mech.* **192**, 577–595.

Counihan, J., Hunt, J. C. R., and Jackson, P. S.: 1974, 'Wakes Behind Two-Dimensional Surface Obstacles in Turbulent Boundary Layers', *J. Fluid Mech.* **64**, 529–563.

Finnigan, J. J. and Bradley, E. F.: 1983, 'The Turbulent Kinetic Energy Budget Behind a Porous Barrier: An Analysis in Streamline Coordinates', *J. Wind Eng. Ind. Aerodyn.* **15**, 157–168.

Finnigan, J. J. and Brunet, Y.: 1995, 'Turbulent Airflow in Forests on Flat and Hilly Terrain', in M. P. Coutts and J. Grace (eds.), *Proc. IUFRO Conf. on Wind and Wind-Related Damage to Trees,* Edinburgh, 1993, pp. 3–40, Cambridge University Press: Cambridge.

Finnigan, J. J. and Mulhearn, P. J.: 1978, 'Modelling Waving Crops in a Wind Tunnel', *Boundary-Layer Meteorol.* **14**, 253–277.

Gandemer, J.: 1981, 'The Aerodynamic Characteristics of Windbreaks Resulting in Empirical Design Rules', *J. Wind Eng. Ind. Aerodyn.* **7**, 15–36.

Guyot, G.: 1986, *Manual sur l'utilisation des brise-vents dans les zones arides,* FAO, Rome.

Guyot, G. and Seguin, B.: 1975, 'Modification of Land Roughness and Resulting Microclimatic Effects: A Field Study in Brittany', in D. A. de Vries and N. H. Afgan (eds.), *Heat and Mass Transfer in the Biosphere, Part I: Transfer Process in the Plant Environment*, Scripta Book Co., New York, pp. 467–478.

Hagen, L. J. and Skidmore, E. L.: 1971, 'Turbulent Velocity Fluctuations and Vertical Flow as Affected by Windbreak Porosity', *Trans. ASAE* **14**, 634–637.

Heisler, G. M. and De Walle, D. R.: 1988, 'Effects of Windbreak Structure on Wind Flow', *Agric. Ecosystems Environ.* **22/23**, 41–69.

Iqbal, M., Khotry, A. K., and Seguin, B.: 1977, 'A Study of the Roughness Effects of Multiple Windbreaks', *Boundary-Layer Meteorol.* **11**, 187–203.

Jackson, P. S.: 1981, 'On the Displacement Height in the Logarithmic Velocity Profile', *J. Fluid Mech.* **111**, 15–25.

Jensen, M.: 1958, 'The Model Law for Phenomena in the Natural Wind', *Igenioren*, Int. Edn. **2**, 121–128.

Kaimal, J. C. and Finnigan, J. J.: 1994, *Atmospheric Boundary Layer Flows: Their Structure and Measurement*, Oxford University Press, Oxford, 289 pp.

Konstantinov, A. R. and Struzer, L. R.: 1965, 'Shelterbelts and Crop Yields', Translated by A. Barach. Israel Program for Scientific Translations, 1969, US Dept. of Commerce. Springfield, Va., 138 pp.

Laws, E. M. and Livesey, J. L.: 1978, 'Flow Through Screens', *Ann. Rev. Fluid Mech.* **10**, 247–266.

Legg, B. J., Coppin, P. A., and Raupach, M. R.: 1984, 'A Three-Hot-Wire Anemometer for Measuring Two Velocity Components in High Intensity Boundary Layers', *J. Phys. E.* **17**, 970–976.

McAneney, K. J. and Judd, M. J.: 1987, 'Comparative Shelter Strategies for Kiwifruit: A Mechanistic Interpretation of Wind Damage Measurements', *Boundary-Layer Meteorol.* **54**, 129–146.

McAneney, K. J. and Judd, M. J.: 1991, 'Multiple Windbreaks: An Aeolian Ensemble', *Agric. For. Meteorol.* **39**, 225–250.

McNaughton, K. G.: 1988, 'Effects of Windbreaks on Turbulent Transport and Microclimate', *Agric. Ecosystems Environ.* **22/23**, 17–39.

Mulhearn, P. J. and Finnigan, J. J.: 1978, 'Turbulent Flow over a Very Rough, Random Surface', *Boundary-Layer Meteorol.* **15**, 109–132.

Nord, M.: 1991, 'Shelter Effects of Vegetation Belts – Results of Field Measurements'. *Boundary-Layer Meteorol.* **54**, 363–385.

Panofsky, H. E. and Dutton, J. A.: 1984, *Atmospheric Turbulence: Models and Methods for Engineering Applications*, Wiley, New York, 397 pp.

Perera, M. D. A. E. S.: 1981, 'Shelter Behind Two Dimensional Solid and Porous Fences', *J. Wind Eng. Ind. Aerodyn.* **8**, 93–104.

Plate, E. J.: 1971a, 'Aerodynamic Characteristics of Atmospheric Boundary Layers', US Atomic Energy Commission, Office of Information Services, Oak Ridge.

Plate, E. J.: 1971b, 'The Aerodynamics of Shelter Belts', *Agric. Meteorol.* **8**, 203–222.

Raine, J. K. and Stevenson, D. C.: 1977, 'Wind Protection by Model Fences in a Simulated Atmosphere Boundary Layer', *J. Ind. Aerodyn.* **2**, 159–180.

Raupach, M. R.: 1988, 'Canopy Transport Processes', in W. L. Steffen and O. T. Denmead (eds.), *Flow and Transport in the Natural Environment: Advances and Applications*, Springer-Verlag, Berlin, pp. 95–127.

Raupach, M. R., Thom, A. S., and Edwards, I.: 1980, 'A Wind Tunnel Study of Turbulent Flow Close to Regularly Arrayed Rough Surfaces', *Boundary-Layer Meteorol.* **18**, 373–397.

Raupach, M. R., Coppin, P. A., and Legg, B. J.: 1986, 'Experiments on Scalar Dispersion within a Model Plant Canopy, Part I: The Turbulence Structure', *Boundary-Layer Meteorol.* **35**, 21–52.

Rogers, M. M. and Moser, R. D.: 1994, 'Direct Simulation of a Self-Similar Turbulent Mixing Layer', *Phys. Fluids* **6**, 903–923.

Ruderich, R. and Fernholz, H. H.: 1986, 'An Experimental Investigation of a Turbulent Shear Flow with Separation, Reverse Flow, and Reattachment', *J. Fluid Mech.* **163**, 283–322.

Schlichting, H.: 1968, *Boundary Layer Theory*, McGraw-Hill, New York, 747 pp.

Seguin, B. and Gignoux, M.: 1974, 'Etude expérimentale de l'influence d'un réseau de brise-vent sur le profile vertical de vitesse du vent', *Agric. Meteorol.* **13**, 15–33.

Sturrock, J. W.: 1969, 'Aerodynamic Studies of Shelterbelts in New Zealand – 1: Low to Medium-Height Shelterbelts in Mid-Canterbury', *N.Z. J. Sci.* **12**, 754–776.

Thom, A. S.: 1971, 'Momentum Absorption by Vegetation', *Quart. J. Roy. Meteorol. Soc.* **97**, 414-428.

Townsend, A. A.: 1976, *The Structure of Turbulent Shear Flow,* Cambridge University Press, Cambridge, 429 pp.

Van Eimern, J., Karschon, R., Razumova, L. A., and Robertson, G. W.: 1964, *Windbreaks and Shelterbelts,* WMO Technical Note No. 59 (WMO No. 147.TP.70), 188 pp.

Wang Zhengquan, Shi Jiachen, and Wang Yehchu: 1990, 'Application of the Boundary Layer Models to Simulate Wind Velocity Profiles of Shelterbelts', in Xiang Kaifu, Shi Jiachen, Baer, N. M., and Sturrock, J. W. (eds.), *Protective Plantation Technology,* Publishing House of Northeast Forestry University, China.

Wilson, J. D.: 1985, 'Numerical Studies of Flow Through a Windbreak', *J. Wind Eng. Ind. Aerodyn.* **21**, 119–154.

Wilson, J. D.: 1987, 'On the Choice of a Windbreak Porosity Profile', *Boundary-Layer Meteorol.* **38**, 37–49.

Wilson, J. D., Swaters, G. E., and Ustina, F.: 1990, 'A Perturbation Analysis of Turbulent Flow through a Porous Barrier', *Quart. J. Roy. Meteorol. Soc.* **116**, 989–1004.

Wooding, R. A.: 1968, 'A Low Speed Wind Tunnel for Model Studies in Micrometeorology. II. The Pye Laboratory Wind Tunnel', Aust. CSIRO Div. Plant Ind. Tech. Pap. No. 25, pp. 1–24.

Woodruff, P. N. and Zingg, A. W.: 1955, 'A Comparative Analysis of Wind Tunnel and Atmospheric Air Flow Patterns about Single and Successive Barriers', *Trans. Amer. Geophys. Union* **36**, 203–208.

Wygnanski, I. and Fiedler, H. E.: 1970, 'The Two Dimensional Mixing Region', *J. Fluid Mech.* **41**, 327–361.

Zhuang, Y. and Wilson, J. D.: 1994, 'Coherent Motions in Windbreak Flow', *Boundary-Layer Meteorol.* **70**, 151–169.